Politecnico di Torino

Master Thesis in
Energetic and Nuclear Engineering

A.y. 2021/2022

CFD Analysis of a Thermocline Storage System with Phase Change Material for CSP Applications

Supervisors:
Prof. Roberto Zanino
PhD Mattia Cagnoli

Candidate:
RICCARDO SISTI

Ringrazio il Prof. Roberto Zanino e il Dr. Mattia Cagnoli per avermi seguito durante tutto lo svolgimento della tesi. A quest'ultimo in particolare sono immensamente grato per avermi costantemente supportato e guidato con chiarezza e puntualità. Il suo interesse e la sua passione per la termo-fluido dinamica sono stati per me fonte di ispirazione, determinando un confronto sempre fruttuoso e decisivo per il proseguimento del lavoro.

Desidero poi porgere i miei ringraziamenti a tutti gli esponenti dell'ENEA: Walter Gaggioli, Valeria Russo e Raffaele Liberatore, che hanno generosamente dedicato del tempo al mio lavoro, mettendomi a disposizione le loro conoscenze e il materiale necessario.

Un sentito ringraziamento va agli amici del gruppo di Chieri, che sono stati sempre presenti nei momenti di gioia e di difficoltà, ai compagni e amici che ho incontrato durante l'intero percorso universitario e a tutti coloro che mi sono stati vicini in questi anni.

Ringrazio infine i miei familiari, grazie ai quali ho potuto dedicarmi a tempo pieno e con serenità durante il mio intero percorso di studi, sapendo che non mi avrebbero mai fatto mancare nulla.

Contents

Supervisors: Prof. Roberto Zanino - Dr. Mattia Cagnoli
Candidate: RICCARDO SISTI

Supervisors: Prof. Roberto Zanino - Dr. Mattia Cagnoli
Candidate: RICCARDO SISTI

Acronyms

Acronym	Description
CFD	Computational Fluid Dynamics
CSP	Concentrating Solar Power
GHG	Greenhouse Gases
PV	Photovoltaic
SM	Storage Medium
HTC	Heat Transfer Coefficient
HTF	Heat Transfer Fluid
HX(s)	Heat Exchanger(s)
IC(s)	Initial Condition(s)
MS	Molten Salts
PCM(s)	Phase Change Material(s)
RES	Renewable Energy Sources
TES	Thermal Energy Storage
STES	Sensible Thermal Energy Storage
LTES	Latent Thermal Energy Storage
ORC	Organic Rankine Cycle
LTES	Latent Thermal Energy Storage
BC(s)	Boundary Condition(s)
CV(s)	Control Volume(s)
VOF	Volume Of Fluid

Supervisors:
Prof. Roberto Zanino - Dr. Mattia Cagnoli
Candidate:
RICCARDO SISTI

Abstract

In the context of concentrating solar power (CSP) systems, the thermocline thermal storage system is a potentially cost-effective alternative to the more common storage system based on two-tank, one hot and one cold. As part of the European ORC-Plus project, ENEA (Italian institute for new technologies, energy and sustainable development) has proposed an innovative molten salt storage system based on the thermocline technology, of which a 1:100 scale prototype has been built at the PCS (Prova Collettori Solari) facility at the ENEA research center of Casaccia. The aim of this thesis is to numerically evaluate the potential of inserting phase change material (PCM) into the tank in terms of thermal performance.

First, a brief introduction is given to the readers regarding the general topic of decarbonisation of the energy sector and the growing importance of low-carbon technologies with a focus on CSP systems. Afterwards, the idea behind the design of the prototype, the experimental campaign and the development of a validated CFD model of the prototype are presented.

Based on this solid basis, the previously CFD model was modified to include inserts filled with phase change materials. To maintain an acceptable computational cost, the domain of the CFD model does not include the tube walls and the PCM, which are replaced by a Robin-type boundary condition governed by a lumped parameter model. To this end, it is also determined in which region of the storage tank it is convenient to insert the PCMs, which phase change material is the most suitable, depending on the melting temperature, and which geometry to adopt for the inserts containing the phase change material.

In conclusion, the CFD model coupled with the lumped parameter model is used to simulate a charging transient and the results are compared with those of the storage system without the PCM inserts. The results show that the phase change material allows the temperature of the salts in the upper part of the tank to be stabilised, also leading to a clearer separation between the hot salts and the rest of the thermocline.

Supervisors:
Prof. Roberto Zanino - Dr. Mattia Cagnoli
Candidate:
RICCARDO SISTI

Estratto

Nel contesto dei sistemi a concentrazione solare (CSP), il sistema di accumulo termico a termoclino è un'alternativa potenzialmente conveniente rispetto al più comune sistema di accumulo basato su due serbatoi, uno caldo e uno freddo. Nell'ambito del progetto europeo ORC-Plus, l'ENEA (Istituto italiano per le nuove tecnologie, l'energia e lo sviluppo sostenibile) ha proposto un innovativo sistema di accumulo a sali fusi basato sulla tecnologia termoclino, per cui è stato costruito un prototipo in scala 1:100 presso la struttura PCS (Prova Collettori Solari) del centro di ricerca ENEA della Casaccia. Lo scopo di questa tesi è quello di valutare numericamente le potenzialità dell'inserimento di materiale a cambiamento di fase (PCM) nel serbatoio in termini di prestazioni termiche.

In primo luogo, viene fatta una breve introduzione ai lettori riguardo al tema generale della decarbonizzazione del settore energetico e della crescente importanza delle tecnologie a bassa emissione di carbonio con un focus sui sistemi CSP. In seguito, vengono descritti l'idea alla base della progettazione del prototipo, la campagna sperimentale e lo sviluppo di un modello CFD convalidato del prototipo.

Appoggiandosi su queste solide basi, il precedente modello CFD è stato modificato per includere gli inserti riempiti con il materiale a cambiamento di fase. Per mantenere un costo di calcolo accettabile, il dominio del modello CFD non ha incluso le pareti del tubo e il PCM, che sono stati sostituiti da una condizione al contorno di tipo Robin governata da un modello a parametri concentrati. A tal fine si è determinato anche in quale regione del serbatoio è conveniente inserire i PCM, il materiale a cambiamento di fase più adatto in base alla temperatura di fusione e la geometria da adottare per gli inserti contenenti il materiale a cambiamento di fase.

In conclusione, il modello CFD accoppiato al modello a parametri concentrati è stato usato per simulare un transitorio di carica e i risultati sono stati confrontati con quelli del sistema di accumulo termico senza gli inserti

PCM. I risultati hanno mostrato che il materiale a cambiamento di fase permette di stabilizzare la temperatura dei sali nella parte superiore del serbatoio, determinando anche una separazione più netta tra i sali caldi e il resto del termoclino.

Chapter 1

1 Introduction

The objective of this thesis is the development of a *Computational Fluid Dynamics* (CFD) model, able to simulate the introduction of *Phase Change Materials* (PCMs) inside an innovative concept of *molten salts thermocline energy storage* with integrated heat exchangers for *Concentrating Solar Power* (CSP) applications. This innovative energy storage has been designed and experimentally tested by ENEA (Agenzia nazionale per le nuove tecnologie, l'energia e lo sviluppo economico sostenibile-Italian institute for new technologies, energy and sustainable development) in the framework of the European Project ORC-Plus [1].

In this chapter, some background information is provided to explain the potential of combining the CSP technology with the thermal energy storage in the future energy scenario.

1.1 Decarbonisation of the Energy Sector

Global warming is a critical and current phenomenon defined as the long-term heating of Earth's climate system observed since the pre-industrial period due to human activities, primarily fossil fuel burning, which increases heat-trapping *greenhouse gases* (GHG) level in Earth's atmosphere. An important percentage of these anthropogenic emissions is related to the energy production,

considering that the 81% of the *world primary energy demand* was still satisfied by fossil fuels in 2019 [2].

The uneven distribution of the fossil fuel deposits increases the concerns about energy security due to their crucial role in the today energy system. From an economic perspective the instability of markets and prices is also a drawback in their use. In addition, they are non-renewable resources which raises the question of their depletion and their availability for this generation and the future ones. All the above mentioned criticalities lead to unsustainable energy systems and to the quest for new solutions for reducing the negative impacts of energy systems [3].

The decarbonization of the energy sector has been the subject of research for several years, gaining increased attention recently. The first worldwide common efforts to control and stabilize the concentration of GHG in the atmosphere took place at the Earth Summit in Rio De Janeiro in 1992, where many countries agreed on the United Nations Framework Convention on Climate Change (UNFCCC). In 2015, with the Paris Agreement, parties to the UNFCCC reached a landmark agreement to combat climate change and to accelerate and intensify the actions and investments needed for a sustainable low carbon future. The central aim was the commitment to *"keeping a global temperature rise this century well below 2 degrees Celsius above pre-industrial levels and to pursue efforts to limit the temperature increase even further to 1.5 degrees Celsius [...] would significantly reduce the risks and impact of climate change"* [4].

The *International Energy Agency* (IEA), every year produces the *World Energy Outlook*, which is a leading source of strategic insight on the future of energy and energy-related emissions, providing detailed scenarios that map out the consequences of different energy policy and investment choices. The *sustainable development scenarios* explains how to reduce drastically the GHG emissions from power production in order to reach the climate goals of the Paris Agreement. To do that, as is shown in **Figure 1.1**, the two actions that have the greatest impact are the improvement in the efficiency of the energy production and the utilization and the deployment of the renewables.

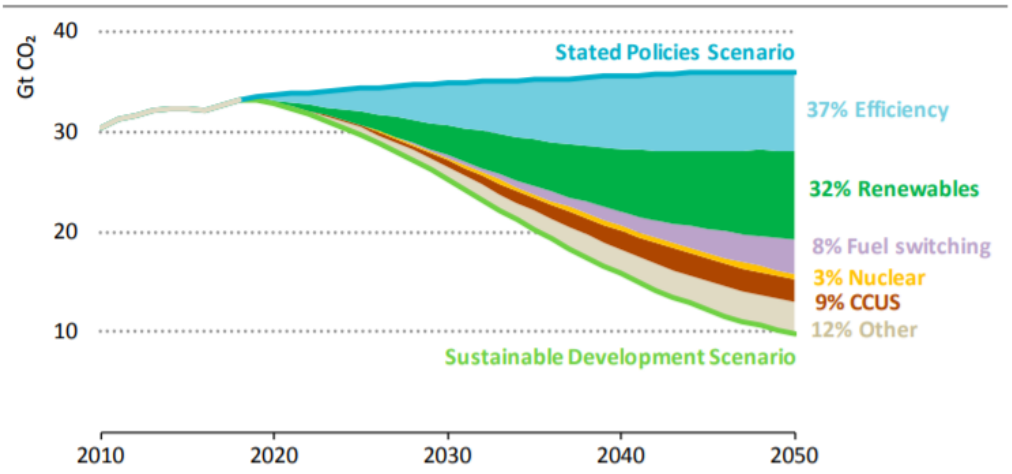

Figure 1.1 GHG emissions forecast in Stated Policies Scenarios and in the Sustainable Development Scenario [2].

1.2 Solar Technologies

Energy from the sun is one of the main sources of renewable energy, the total annual solar radiation falling on the earth is more than 7500 times the world's total annual primary energy consumption of 450 EJ registered in 2013 [5].

There are several ways to exploit the solar energy to produce heat, electricity or a combination of them. *Low-temperature solar thermal panels* convert the energy of the solar irradiation in thermal energy by heating a heat transfer fluid (HTF) up to about 100 °C. This technology is typically adopted in heating and cooling systems for buildings, domestic hot water and industrial process heat.

Photo-Voltaic (PV) technologies covert the absorbed sunlight energy into electricity. A PV cell is made from semiconductor materials with a p-n junction. A photon, which is absorbed by the cell, produces an electron hole pairs in the cell and, if an external circuit is formed, the voltage difference drives the electrons from the n-side to the p-side of the junction forming electric current in the external circuit. The main drawback of this technologies is the intermittency and unpredictability of the solar energy, not only at night but also during the daytime. Coupling the PV cells with batteries is the most commonly used

Supervisors:
Prof. Roberto Zanino - Dr. Mattia Cagnoli
Candidate:
RICCARDO SISTI

solution to prevent those problems but the investment cost increases considerably.

Concentrating solar power (CSP) are based on the concept of concentrating solar radiation to heat up an HTF, that is then exploited to drive a thermodynamic cycle (typically a Rankine cycle) for electricity production. The main advantage of this technology is the possibility of storing the thermal energy or even use it for district or industrial heating applications.

The spread of this technologies is continuously growing in the last 15 years and this trend is expected to be confirmed in the next years as shown in the **Figure 1.2**. From the graph, it can be seen that the portion of concentrated solar technology is still limited and not clearly visible compared to the others.

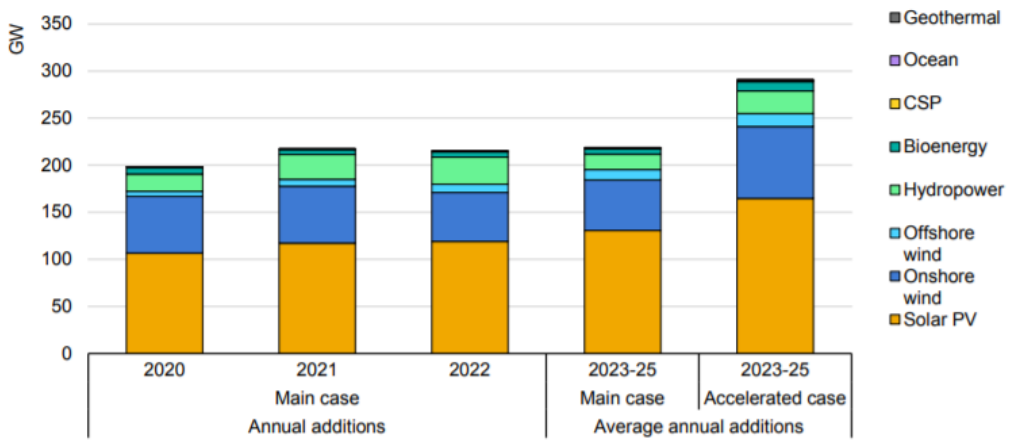

Figure 1.2 Renewables spread and forecast to 2025 [6].

The photovoltaic, but also wind power, are the leading technologies in terms of new installation. The International Energy Agency (IEA) estimates, in the main case, a total wind and solar capacity doubling [6]. With this growth, wind and PV achieve two important targets: their total installed capacity surpasses that of natural gas in 2023 and that of coal in 2024. Overall, renewables account for 95% of the increase in total power capacity through 2025 [6].

1.2.1 Critical Aspect

As show in **Figure 1.2** solar PV and wind power are the *renewable energy sources* (RES) with highest spread in the world. The grid cannot rely on these technologies because of their *intermittency* and operator must adjust the day-ahead plan to include power plants, such as turbogas power plants, that can quickly adjust their power output to compensate for the rise and fall in RES generation, while the base-load is generally met by large-scale hydroelectric, coal, natural gas and nuclear power plants because they are designed to operate continuously producing electricity at the lowest cost. To compensate the fluctuating nature of the RES, energy storage systems have been introduced, but they could be expensive, especially for large-scale capacities [7].

Other issues regard specifically the PV penetration are highlighted by the *duke curve* represented in **Figure 1.3** [8]. The chart illustrates for each line the net load, equal to the normal load minus wind and PV generation between 2012 and 2020. The first challenge with high solar adoption is the potential for PV to produce, in the central hour of the day, more energy than can be used at one time, called *over-generation*. This leads system operators to curtail PV generation, reducing its economic and environmental benefits. The second issue, that is at least as critical as the previous one, is the so-called *evening ramp* cause the necessity for conventional generation plant to quickly ramp up energy production when the sun sets and the contribution from PV falls.

Supervisors: Prof. Roberto Zanino - Dr. Mattia Cagnoli
Candidate: RICCARDO SISTI

1. Introduction

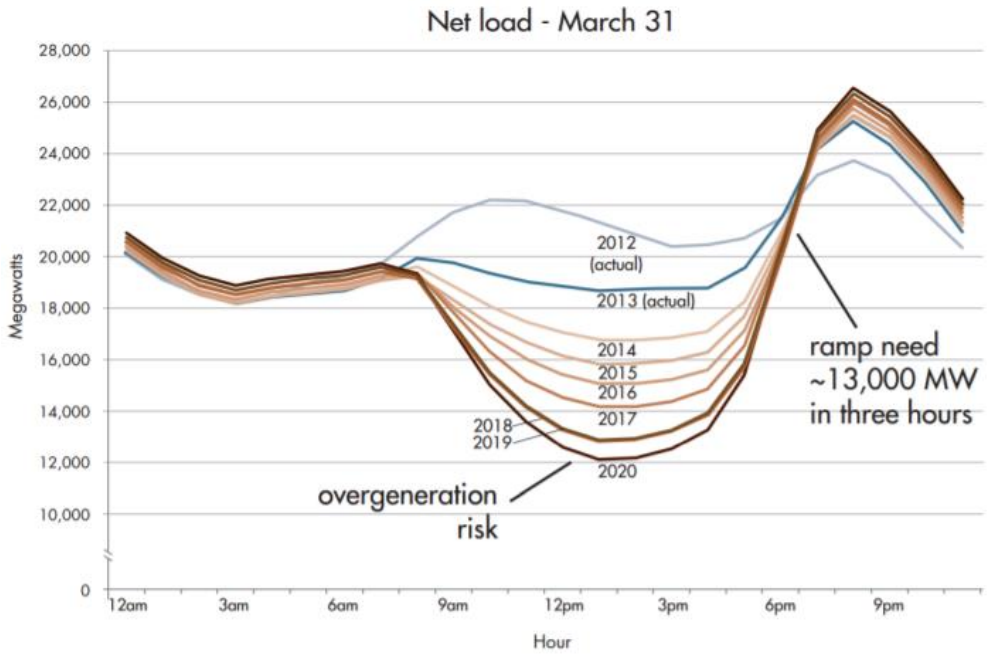

Figure 1.3 Predicted "Duck Curve" evolution in California [8].

The two main solutions to mitigate these problems are to store energy during peak generation and then use it during peak demand but as mentioned above it is still not cost effective. The second is to decrease peak loads by increasing loads during generation by introducing, for example, *time-of-use tariffs*. This solution has the potential to shift loads that are not so time critical to times when the PV is generating [9].

On the side of supply instead, CSP integrated with *Thermal Energy Storage* (TES) can be an optimal solution: a large fraction of the value of this technology derives from its ability to provide firm system capacity [10] and electricity at low cost compared to PV integrated with battery storage [7]. A fraction of the conventional base-load plants could be potentially replaced by a renewable source of dispatchable energy. The characteristics of this technology are then presented in the next section.

1.3 Concentrating Solar Power (CSP) Technology

A CSP plant uses the heat provided by the solar irradiation concentrated in a small area to generate electricity. Using mirrors, the sunlight is focused on a receiver that transfers the energy of the concentrated solar radiation to a heat transfer fluid, which can be exploited to charge a thermal energy storage or directly to drive a convectional thermodynamic cycle for power production.

Solar thermal technologies require direct sunlight, called *direct normal irradiation* (DNI) that represents the intensity per unit surface normal to solar radiation prior to scattering. Suitable sites (**Figure 1.4**), in terms of the energy per unit surface that reaches directly the earth for every year, must get at least $2000\ {}^{kWh}/_{m^2y}$, while the best sites are irradiated by $2800\ {}^{kWh}/_{m^2y}$. Typical locations are characterized by low latitude within 40 degrees north or south and that lack atmospheric humidity, dust and fumes. The potential of this technology in this region is very high and the growth in the future appears clear, taking into account that it is possible to produce 100–130 GWh electricity in one square kilometre of land. This corresponds to the power produced by a 50 MW conventional coal- or gas-fired mid-load power plant [11].

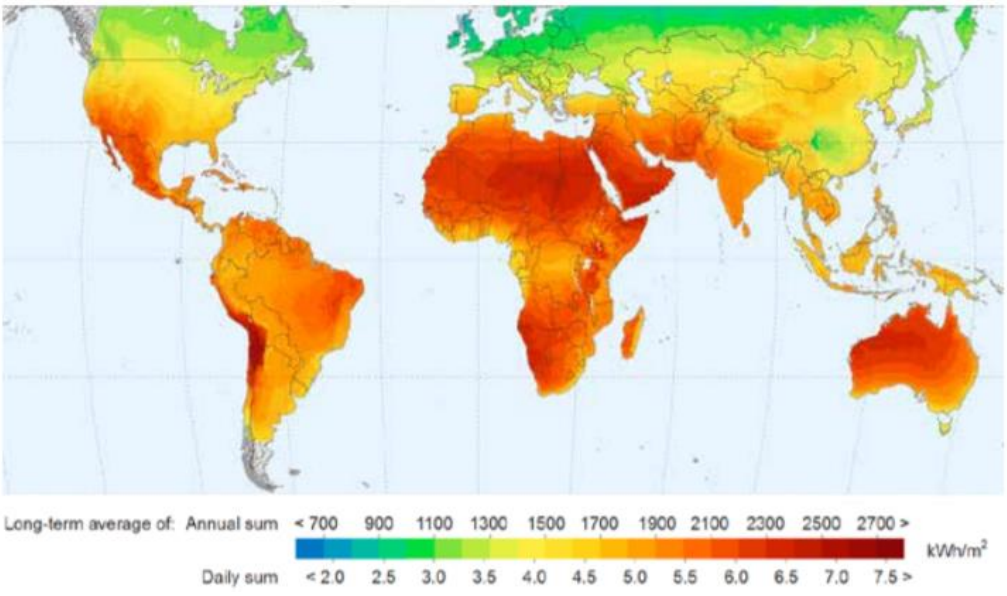

Figure 1.4 Direct normal irradiation world map [11].

1. Introduction

Over the years, several concentrating technologies have been developed as show in **Figure 1.5**: parabolic through collector and linear Fresnel reflector, which are *line-focusing system*, and solar power tower and parabolic dish systems that are *point-focusing system*. The choice of the concentration method characterized the plant in terms of temperature, pressure, efficiency, costs, materials, power cycle and land occupancy. Usually, comparing linear and tower systems results in lower temperatures, efficiency and costs in the former, but the environmental impact is much higher in the latter.

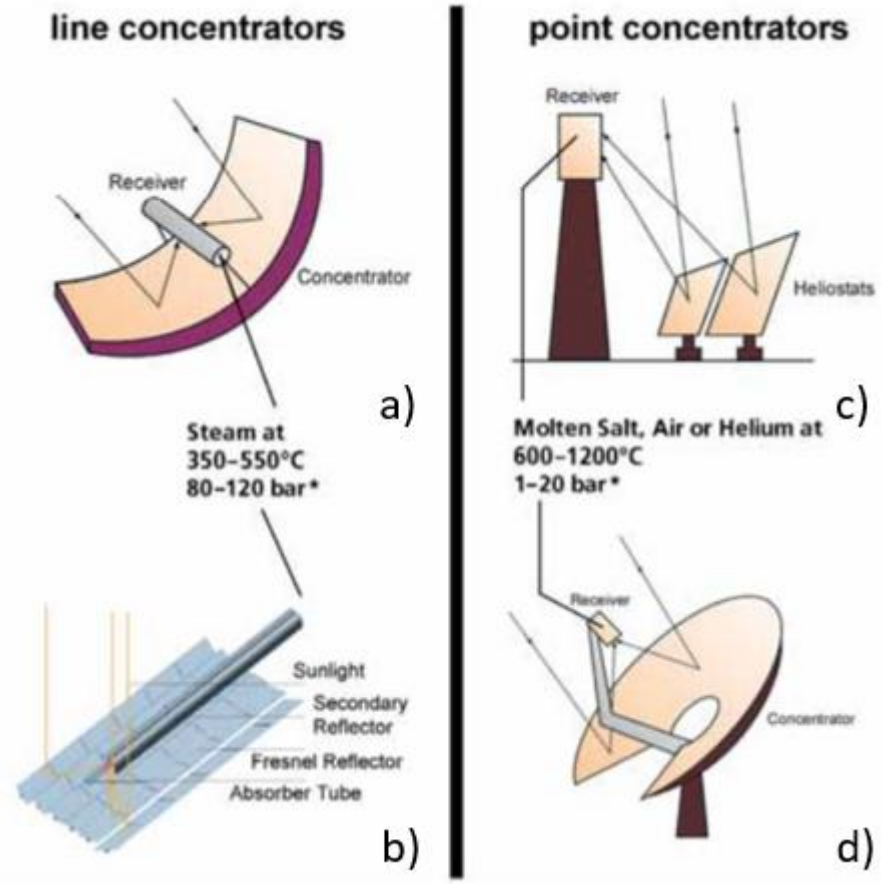

Figure 1.5 Representation of the different concentration technologies: a) is the parabolic through collector, b) is the linear Fresnel reflector, c) is the solar power tower and d) is the parabolic dish system.

The other two main components of a CSP plant are the *power block* and the *thermal storage system*. Regarding the conversion of the thermal energy in power, different choices can be made depending mainly on the temperature level.

The most common cycles adopted in the CSP plants are: the *Rankine (steam) cycles*, *Organic Rankine Cycle* (ORC), the *Stirling cycle* and the *Brayton cycle* [12].

The role of the *thermal storage system* is to store the thermal energy produced during the sunny hours, which can be exploited when the solar radiation is low or absent, keeping a constant power generation. An in-depth description of the thermal storage systems is provided in the next chapter.

1.4 Thermal Energy Storage (TES)

As previously mentioned, the possibility of storing thermal energy allows producing electricity even in the absence of the sun. Therefore, integrating a TES system in the CSP technology permits the optimization of electricity resale and production. The development of an efficient and cost-effective TES system is crucial for the future of CSP technologies. An energy storage system can be described in terms of the following characteristics [13]:

- **Capacity**: defines the energy stored in the system and depends on the storage process, the medium and the size of the system.
- **Power**: defines how fast the energy stored in the system can be charged or discharged.
- **Efficiency**: is the ratio of the energy provided to the user to the energy needed to charge the storage system.
- **Storage Period**: defines how long the energy is stored and lasts from hours to months.
- **Charge and Discharge Times**: defines how much time is needed to charge/discharge the system.
- **Cost**: Depends on the capital and operation costs of the storage equipment and lifetime.

There are currently three kinds of TES system available: *sensible heat storage*, *latent heat storage* and *thermochemical heat storage*. A description of the first two technologies is detailed in the next sections.

1.4.1 Sensible Thermal Heat Storage (STES)

Sensible Thermal Energy Storage (STES) is the most developed technology that has been studied, tested and installed [14]. STES method is based on storing/releasing thermal energy thanks to the temperature change of the storage medium. The main parameters are the heat capacity and the density of the material [14].

A first categorization can be done distinguishing *storage medium* in solid and liquid form. Solid materials have a wide range of operating temperatures, high thermal conductivity and relatively low cost. Liquid materials are also widespread; especially molten salts are considered as one of the best materials for CSP applications since their features include high heat capacity, excellent thermal stability at high temperatures, low vapor pressure, low viscosity, high thermal conductivity, nonflammability and non-toxicity.

A second categorization can be done distinguishing between *direct thermal storage*, where the storage and HTF for a given system are the same, or *indirect thermal storages*, where they are different. The amount of stored thermal energy in system based on the sensible heat depends on the specific heat capacity, on the temperature change and on the amount of the *storage medium* (SM):

$$Q = M_{SM} \int_{T_{start}}^{T_{end}} c_{SM}(T) dT \qquad (1)$$

Where M_{SM} is the SM mass, c_{SM} is the specific heat of SM and T is the temperature of the storage medium.

During a design of a STES, the selection of the storage material is one of the main and most critical aspects to be considered. In fact, when dealing with the cost of a thermal storage system, the huge amount of SM required is the main voice.

Today, the most mature solution for the TES is represented by the *two-tank system* [15], which consists of a low-temperature and a high-temperature tank.

To reduce the cost of the TES, the two-tank configuration can be replaced by a *thermocline system* based on a *single-tank* where the high temperature zone is separated from the low temperature zone by a thermal gradient.

Two-Tank Configuration

The two-tank TES configuration is the most common; the hot tank is located at the receiver outlet to store energy at high temperature, while the cold tank is located at the receiver inlet to store energy at about the temperature of the heat transfer fluid entering the receiver. Two possible setups for coupling the TES with a CSP system are possible: direct and indirect (**Figure 1.6**).

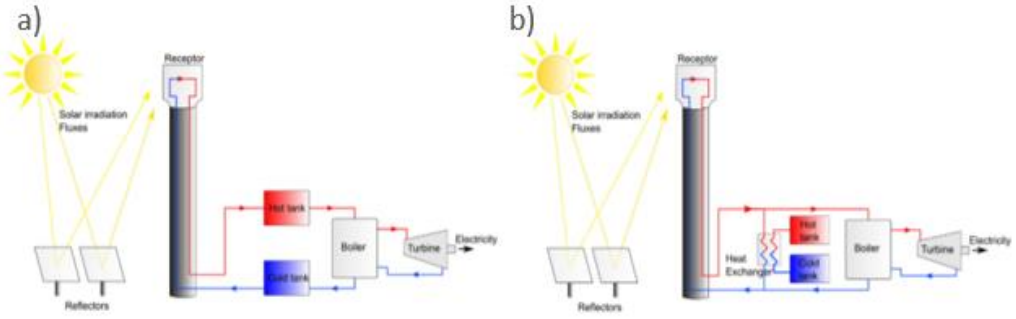

Figure 1.6 CSP system equipped with a two-tank TES: a) direct and b) indirect configurations [14].

The latter is the most common [16], which adopts different fluids in the receiver (heat transfer fluid) and in storage tanks (storage medium). The heat transfer fluid is typically a thermal oil, while the molten salts is used as storage medium. The storage medium from the low-temperature tank flows through a heat exchanger (HX), where it is heated by the high-temperature heat transfer fluid. The high-temperature storage fluid then flows back to the high-temperature storage tank. The fluid of the solar loop exits from the heat exchanger at a low temperature and returns to the solar collector or receiver, where it is heated back to a high temperature. Storage fluid from the high-temperature tank is used in the power block for electricity production and returns to the low-temperature tank [13]. The advantage of this option is the relatively low cost of the components of the oil circuit, whilst the disadvantage is that the

highest temperature is limited to around 390°C by the thermal oil maximum temperature.

On the other hand, a direct system has only one circuit and the solar salt are used both as HTF and as SM. The fluid from the low-temperature tank flows through the receiver, where it is heated up by the concentrated solar radiation, and then it flows to the high-temperature tank. Fluid from the high-temperature tank close the loop in the same manner as the two-tank indirect system [13]. This configuration allows achieving higher temperature and, consequently, storing a same amount of thermal energy with a smaller quantity of SM. However, this configuration implies higher costs for the circuit components that have to cope with higher temperatures and salt corrosion.

Single Tank Configuration: Thermocline Storage

The thermal energy storage is responsible of about 20% of the cost of the entire CSP plant; therefore, a cost reduction would be advantageous making larger storages convenient, with benefits electricity cost wise [17]. It has been assessed that a single-tank configuration has an investment cost up to 33% lower than a two-tank system with the same energy capacity [18], but that requires a very accurate design and operation control in order to work effectively.

The technology that allows the use of a single-tank TES is the thermocline. The word thermocline is from oceanic language. It designates the thermal transition zone between the superficial waters and the deep waters. At the top and the bottom of thermocline zone, temperatures are quasi-uniform, while the difference of temperature is important in the thermocline region.

In a thermocline storage, both the hot and the cold fluid are contained in the same tank: at the top and the bottom temperatures are quasi-uniform, they are separated by a *thermal stratification* due to the buoyancy forces. The region where the thermal gradient occurs is called thermocline (**Figure 1.7**).

1. Introduction

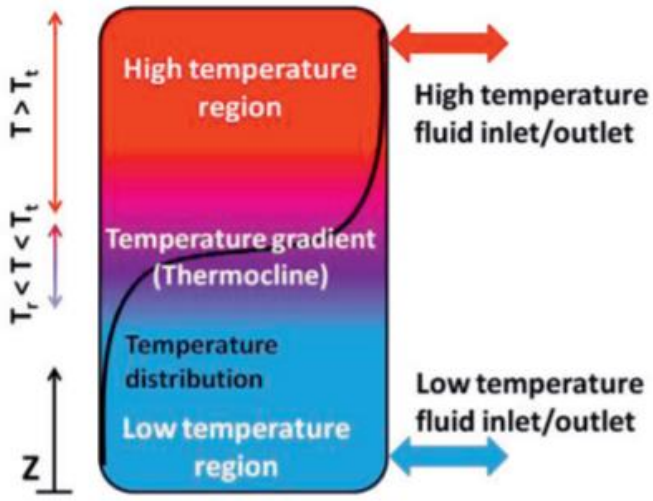

Figure 1.7 Sketch of thermocline energy storage [17].

The ideal condition is to emulate the two-tank configuration in which the hot and cold zones are separated by a zero-height thermocline layer. This is because the *degradation of the stored energy* that can be assessed through an exergy analysis as proposed by Rosen et al. [19]. Considering a thermocline TES with fixed extreme temperatures and a given amount of stored energy, they demonstrated that the exergy increases if the thermocline zone decreases. Moreover, for the same amount of stored energy, exergy content increase as level of stratification (i.e. $T_{max} - T_{min}$) increase.

Four primary contributions to the degradation of the stored energy have been identified in the paper:

- Heat losses to (or leakages from) the surrounding environment.
- Heat conduction from the hot portions of the storage fluid to colder portions.
- Vertical conduction in the tank wall.
- Mixing during charging and discharging periods.

The contributions listed above generate another well-known macro phenomenon that causes thermal energy degradation called thermal hysteresis. It is the progressive degradation of the thermocline after many cycles of operation (**Figure 1.8**).

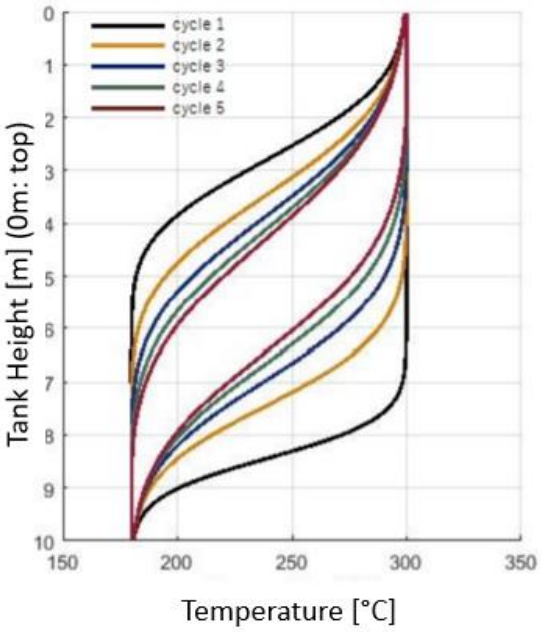

Figure 1.8 Thermocline hysteresis [20].

Scientific researches have proposed different configurations over the years to improve thermal stratification, which, as for the two-tank system, can be direct or indirect.

1.4.2 Latent Thermal Storage (LTES)

Latent thermal energy storage (LTES) systems using *phase change materials* (PCMs) are an effective way of storing thermal energy by exploiting changes in physical state from solid to liquid, liquid to gas or vice-versa. This is because evaporation and condensation allow exploiting the latent heat in addition to the sensible heat, increasing in this way the potential storage capacity. A drawback of the transition of phase is the change in the PCM volume that can cause containment problems. The most widely used solution is the *solid-to-liquid transition*, which, while having a lower latent heat, involves only a small change in volume (<10%), making it economically attractive for use in TES [21].

The main characteristic of a phase change material is the specific latent heat (L), which expresses the amount of heat required to complete the phase change of a unit of mass. The storage capacity in of a PCM medium is given by:

$$Q = M_{PCM} \int_{T_{start}}^{Tmelting} c_{p,solid} dT + M_{PCM} L + M_{PCM} \int_{Tmelting}^{Tend} c_{p,liquid}\, dT \quad (2)$$

Where M_{PCM} is the mass of the PCM, c_p is the specific heat (solid or liquid state) and T is the temperature of the PCM.

The growing interest on LTES is due to its ability to provide high energy storage density, its characteristics to store heat at constant temperature and the abundance and easy availability of low-cost PCMs. Several PCMs are available, which data can be easily found in literature, making possible to identify the most suitable PCM for a specific application on the base of its melting temperature. However, many problems are encountered with PCM due to low thermal conductivity, variation in thermo-physical properties under extended cycles, phase segregation, subcooling, incongruent melting and volume change [21].

The low thermal conductivity determines the need to conduct a detailed analysis to design an optimized heat exchanger in order to effectively transfer the thermal energy from the HTF to the PCM during the charging transient and from the PCM to the HTF during the discharging transient.

1.5 Aim of the work

In this thesis work an innovative design solution proposed and patented by ENEA has been studied. It consists of an indirect TES system where the HTF (a mineral oil) flows into two heat exchangers located inside a special shell that crosses the thermocline layer in the vertical direction. The study focused on the effect on the thermal performance due to the introduction of *phase change material* (PCM) inside the tank through a CFD model capable to reproduce the evolution of the charge transient. It is reported a complete explanation of the

whole system, starting from the choice of the PCM, passing through the optimization of the heat exchanger and ending with the integration of the latent storage system inside the TES thermocline designed by ENEA.

The development of the final model involves the validation of numerical models against experimental data and references from the literature. Finally, the results of the model integrated by phase change inserts are compared with those of the configuration without PCM.

Chapter 2

2 ENEA thermocline concept

The innovative molten salts storage system has been designed by ENEA in the framework of the ORC-Plus (Organic Rankine Cycle – Prototype Link to Unit Storage) European Project [1]. It has been developed to ensure an additional 4 hours of power supply to 1 MWe ORC turbines during the sunless period. The solar field, which provides the thermal energy to the storage system, consists of a linear Fresnel system cooled by a mineral thermal oil, which is the HTF. In order to evaluate the behaviour of the tank in different operating conditions, ENEA presented a preliminary one-dimensional finite differences numerical model [22]. In addition, a prototype of reduced scale (1:100) has been designed and assembled at the *Casaccia Research Center* (Rome, Italy).

The main purpose of this prototype is to experimentally prove the feasibility of the innovative thermocline technology concept [23].

In the following sections, besides the design and working principle of the tank, the characteristics of the testing circuit and of the experimental data will be also presented.

2.1 Description of the prototype

The prototype is a cylindrical tank of height 3088 mm and diameter of 1700 mm filled by molten salts with a volume of about 2.63 m^3. It has a storing

capacity of 200 kWh_{th} by design and it works at atmospheric conditions because of the presence of an open flange on the roof. Its peculiarity, which makes it an innovative technology in the panorama of thermoclines, is the internal channel that connects the two integrated heat exchangers. Referring to **Figure 2.1**, the main components are listed including also their characteristics and materials.

Main Components

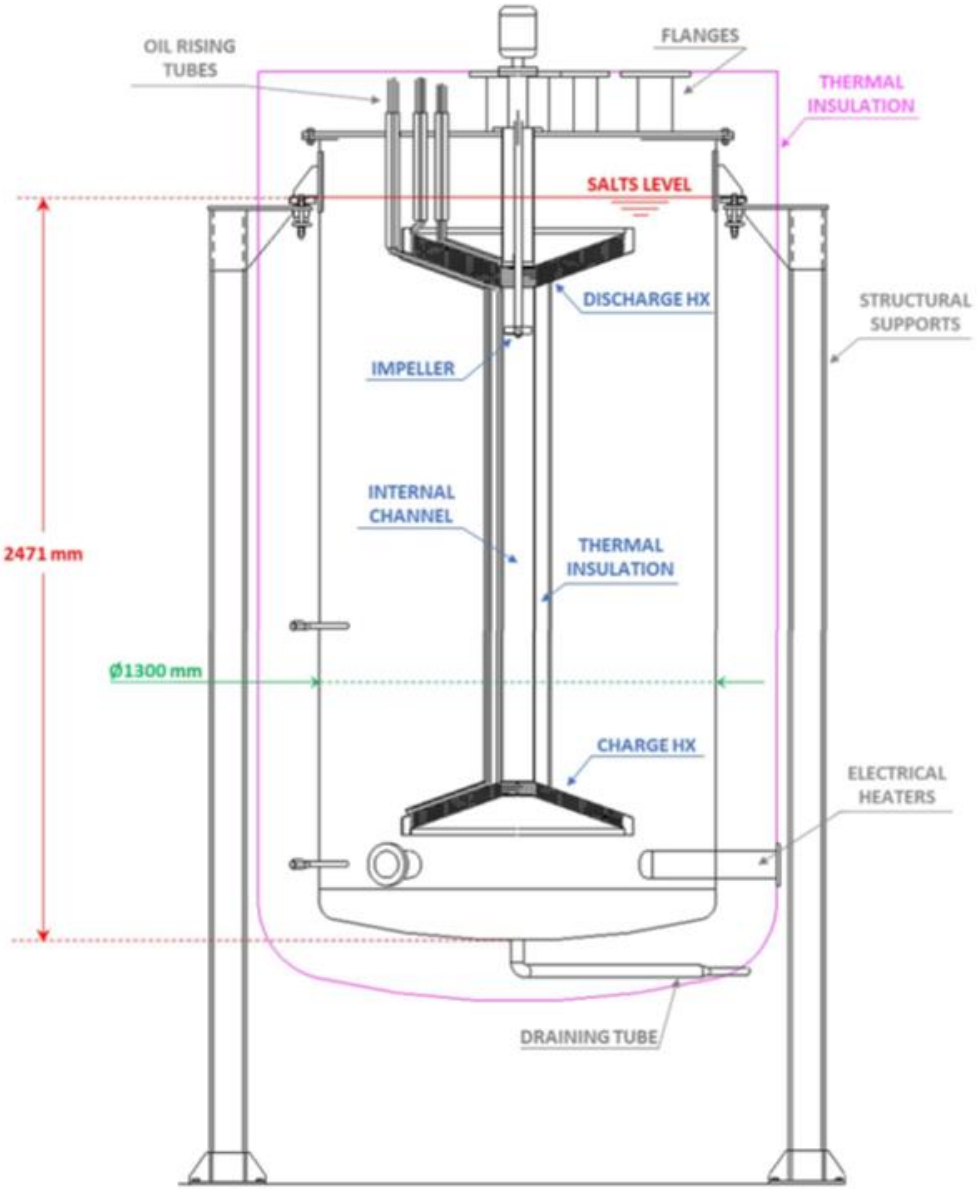

Figure 2.1 Thermocline TES scheme: main components.

Supervisors: Prof. Roberto Zanino - Dr. Mattia Cagnoli
Candidate: RICCARDO SISTI

- **Charge Heat Exchanger**: the internal flow consists of the hot diathermic oil coming from the solar field. The *Heat Exchanger* is made of 4 parallel serpentines (Ø 9.525 mm) of 28 loops each with a conical coil evolution (aperture angle 140°). It is located inside the internal channel at the tank bottom, where the salts temperature is the lowest due to the thermal stratification (**Figure 2.2**).
- **Discharge Heat Exchanger**: it consists of 6 parallel serpentines (Ø 9.525 mm) of 28 loops each having a conical coil evolution. There are two more coils since the amount of energy collected during the whole daytime through the charge HX should be discharged in just four evening hours. The cold diathermic oil coming from ORC cycle flows inside the serpentines. The HX is located in the internal channel at the tank top (**Figure 2.2)**, where the salts temperature is the highest due to the thermal stratification.
- **Internal Channel**: it is a Ø 4" tube lying on the tank axis, with the two extreme sides having a conical shape in order to host the heat exchangers (**Figure 2.2**). The molten salts move from the bottom to the top (charge phase) and vice versa (discharge phase) flowing in the channel. This allows enhancing the thermal stratification in the storage since the channel is thermally insulated and, therefore, the movement of the heated (or cooled) salts does not perturb the salts temperature stratification.

2. ENEA thermocline concept

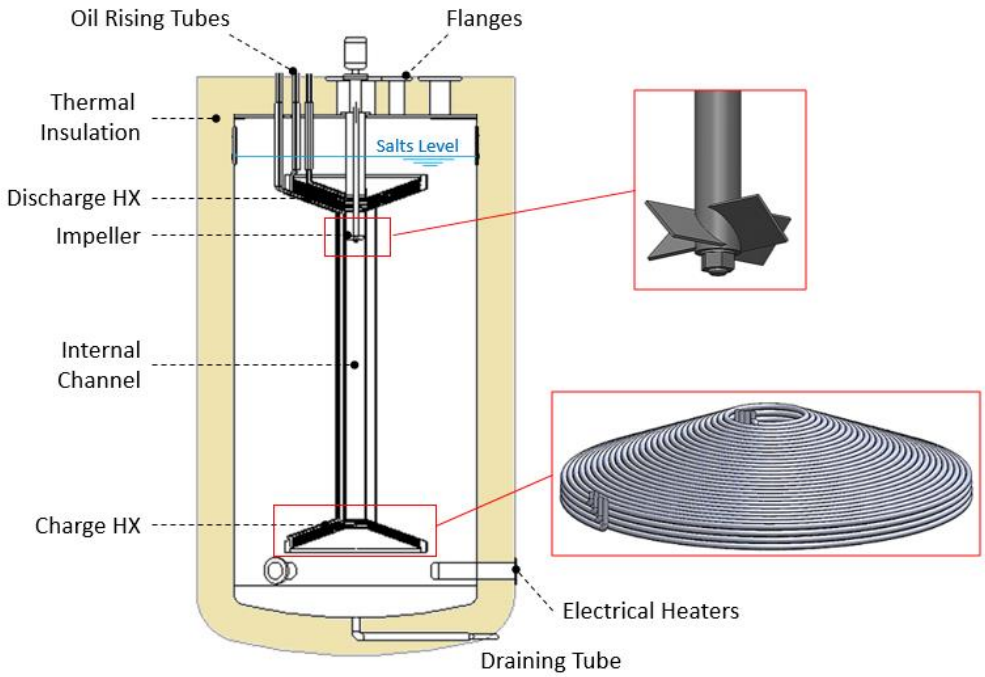

Figure 2.2 Rendering of the main structure of the tank and details on HX and internal channel.

- **Impeller**: it is a shaft equipped with 4 blades inclined at 45° at the end. It is driven by its own motor and can rotate in both directions, with the objective of regulating the flux of molten salts in the channel during the operation.
- **Oil rising tubes**: they have the task of carrying the thermal oil to the heat exchangers and are thermally insulated from the salts.
- **Flanges**: various flanges are needed for different measuring and operative instrumentations creating significant discontinuities in the upper thermal insulation of the tank.
- **Electrical heaters**: two electrical heaters are available to satisfy two main purposes: to compensate the thermal losses avoiding the freezing of the molten salts and to reach the desired initial conditions of temperature inside the tank before of the tests.
- **Structural supports**: they sustain the weight of the tank and keep it in position, lifted from the ground.

Materials

The loop uses the same HTF of the real plant in Benguerir that is the mineral oil called DelcoTerm® Solar E 15. The Hitec XL© is used as SM due to the efficient thermal properties and to meet the constraints of the linear Fresnel operating conditions: the tank has to operate below the maximum oil temperature of 300°C, and then low temperature melting molten salts were necessary. Hitec XL© is a ternary mixture of 15wt% of NaNO3, 43wt% of KNO3 and 42wt% of Ca(NO3)2 after water evaporation [24].

Table 2.1 List of the materials involved in the thermocline TES system proposed by ENEA.

MATERIAL	COMPONENTS
Hitec XL©	Molten salts
DelcoTerm® Solar E 15	Diathermic oil
Rockwool	External thermal insulation: vertical and bottom part
Cerablanket®	External thermal insulation: upper part Internal channel thermal insulation
AISI 316 (austenitic steel)	Heat exchangers/oil rising tubes Impeller Internal channel Tank body Flanges
Carbon steel/Stainless steel	Structural supports

2.2 Experimental Campaign

The specific working principle of the prototype is based on the particular concept of *integrating heat exchangers* connected by the *internal channel*, which aims at improving the thermal stratification thanks to the characteristic path followed by the molten salts during both charging and discharging operations.

During *charge transients*, hot oil enters the bottom heat exchanger from the top and exit from the bottom resulting in a countercurrent configuration. The molten salts around it are heated, reducing their density, and begin to move up driven by buoyancy forces. When the motion is fully developed inside the thermocline, a circular path is obtained: upward in the central duct and downward outside it.

On the contrary, *discharge transients* have the cold oil moving from the top to the bottom of the heat exchanger, again resulting in countercurrent. The molten salts around it cools down, their density increase and they are forced to move downwards by buoyancy forces.

The role of the *impeller* should be those of helping or contrasting the buoyancy driving force, in order to obtain the desired flux inside the internal channel. A better setting of this component is necessary because, as highlighted by the experimental results, it does not yet work properly, destroying the internal stratification.

2.2.1 Experimental Data

To assess and characterized this TES concept a pilot plant was carried out which is able to reproduce the real *operating conditions* in the CSP plant of Benguerir (Morocco). Particular attention is paid to the diagnostic tools used to analyse the experimental behaviour of the prototype and which will be equally reproduced on the CFD model.

- **Temperature stratification**: it is measured by 12 thermocouples, placed 440 mm away from the axis of the tank: 11 recording molten salts temperature and 1 recording air temperature above them. The thermocouples are equally spaced along the tank axis direction but only the distance between them is known and not the height of the first thermocouple, assuming it equal to 101 mm.
- **HX interface thermocouples**: for both the charge and discharge heat exchangers, two thermocouples are installed at the interface with the bulk

molten salts, displaced one another of 180° along the azimuthal direction. They permit to measure the temperature of the molten salts at the inlet/outlet of the channel.

- **Oil side characterization**: the oil flow is characterized by a mass flowmeter on the circuit and by a thermocouple installed at both the inlet and the outlet sections of the charge and discharge heat exchangers.
- **Molten salts mass flowrate**: no instrumentation is applied to detect the mass flow rate of molten salts inside the internal channel. The only way to assess it is by an indirect method through a simplified stationary power balance:

$$\dot{m}_{MS,exp} = \frac{\dot{m}_{oil} \int_{T_{oil,out}}^{T_{oil,in}} c_{p,oil}(T)dT}{\int_{T_{MS,in}}^{T_{MS,out}} c_{p,MS}(T)dT} \quad (3)$$

Where $\dot{m}_{oil}$ is the mass flowrate of the diathermal oil, $c_{p,oil}$ and $c_{p,MS}$ are respectively the specific heat of the diathermal oil and molten salts and, finally, T_{oil} and T_{MS} with the subscripts in and out are respectively the inlet and outlet temperature of the diathermal oil and molten salts for the heat exchanger.

Supervisors: Prof. Roberto Zanino - Dr. Mattia Cagnoli
Candidate: RICCARDO SISTI

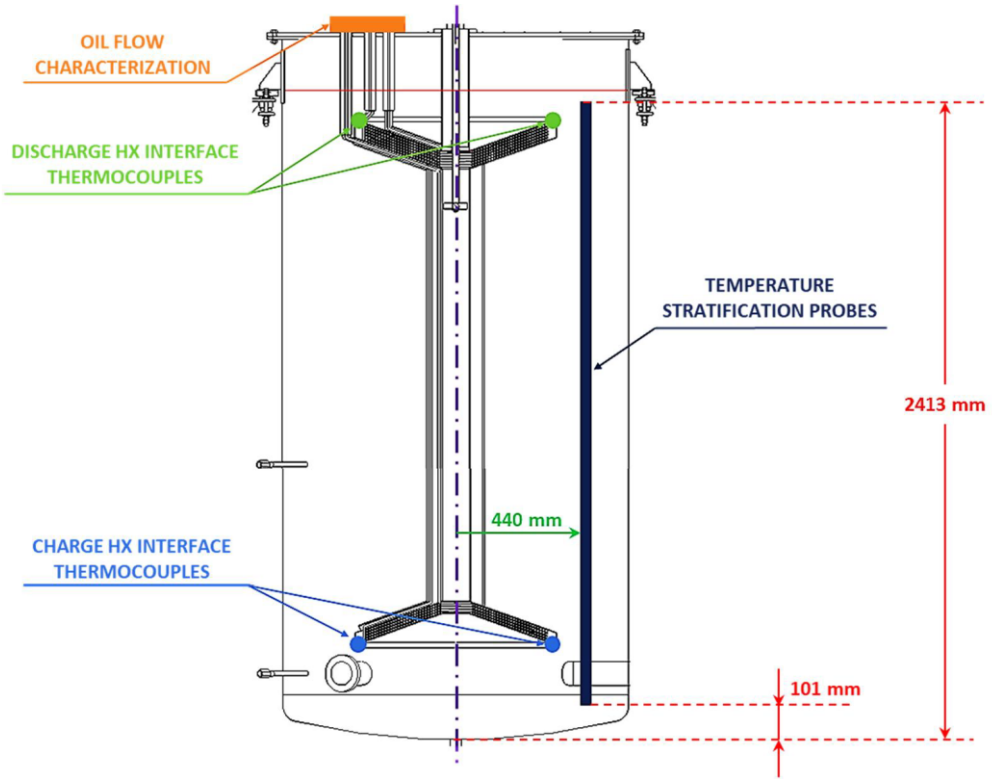

Figure 2.3 Scheme of the main measuring instrumentations installed.

The tests were carried out in January 2019 at the ENEA Casaccia Research Center. A data acquisition system able to collect the data from each installed sensor every 5 seconds was used. The main operating conditions have been reproduced, performing in particular 7 discharge tests, 3 charge tests and 1 no-load test in order to assess the thermal losses. The most representative outcomes are shown in the next section, which are correspond to the salts temperature evolution at different heights from the tank floor.

Charge Test

Different tests have been carried out, the first of which immediately brought to the attention of the problems related by the impeller activation: it is not able to reduce the molten salts flow, creating strong perturbations in the tank destroying the previously set stratification. So, the following test, was performed without using the impeller. Initial conditions are not perfectly homogenized highlighting that three initial temperatures in the bottom of the tank were lower than the others. The cause of this problem is the electric heater used to bring the

salts to the initial temperature, which is located at a higher height than the bottom of the tank. During the transient, it can be seen that only the temperature corresponding to the lowest thermocouple presents abnormal behaviour. The cause is always the height of the thermal driver, which, in this case, is the charge heat exchanger. This criticality is of considerable importance because it implies that a part of the salts mass at the tank bottom side is not recirculated during the transients due to the buoyancy-forces. The measured salts temperature distribution inside the tank during the charge transients (see an example in **Figure 2.4**) make evident that the desired maximum temperature (285 °C) was far from being reached.

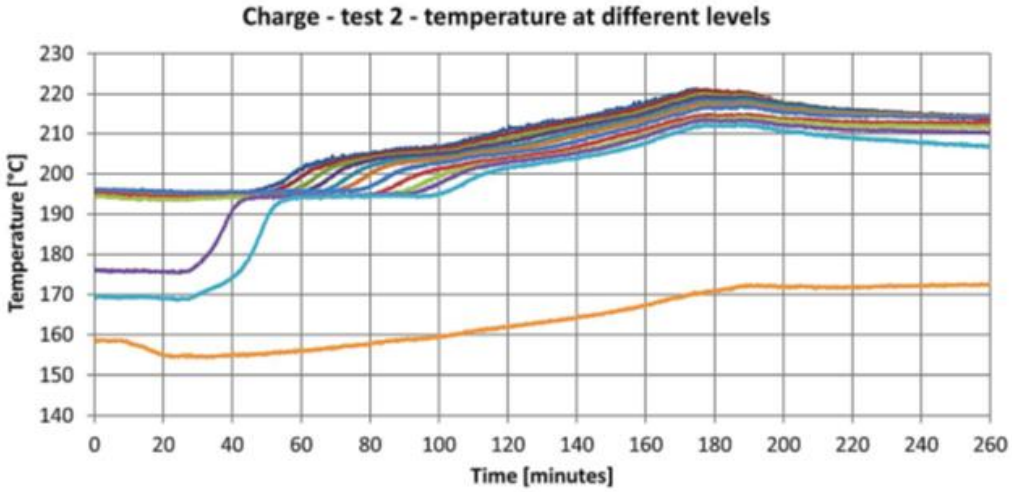

Figure 2.4 Salts temperature evolution for each thermocouples during the charge test 2.

Discharge Test

In the discharge test the initial conditions are reached thanks to the integrated electrical heaters. The tests aim to heating up the oil above the temperature of 260°C (required to drive the ORC cycle), and contextually to discharge completely the storage until the minimum salts temperature (190 °C).

Figure 2.5 shows that the salts are able to heat the oil well above the target temperature of 260°C, but far from reaching the final condition. Also in this test, the impeller was kept switched off.

Supervisors:
Prof. Roberto Zanino - Dr. Mattia Cagnoli
Candidate:
RICCARDO SISTI

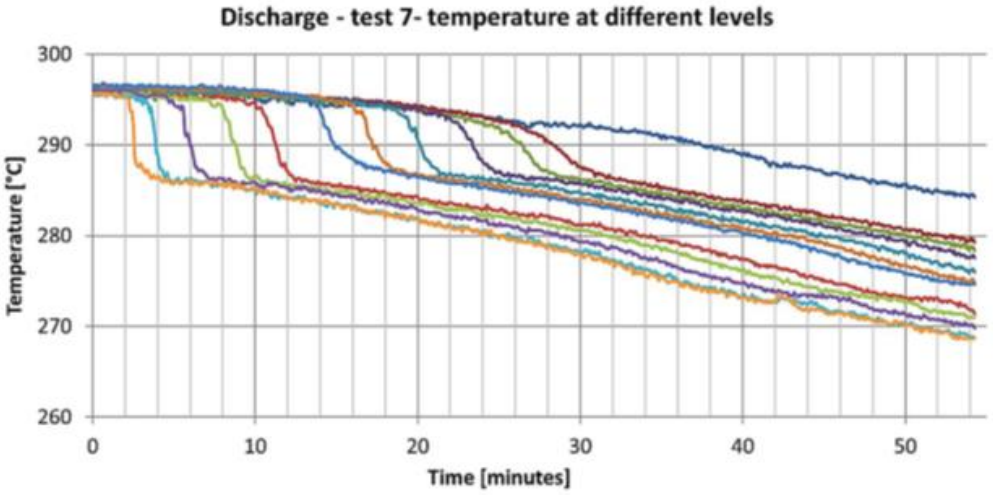

Figure 2.5 Salts temperature evolution for each thermocouples during the discharge test 7.

No-Load Test

The objective of this test was to evaluate the thermal losses towards the environment, starting from an initial condition of uniform temperature of about 263°C. The tank was left without any heat load for almost 18 hours. In the **Figure 2.6**, the results have been presented by evaluating the average temperature among all thermocouples, the latter being considered more representative for the analysis under consideration.

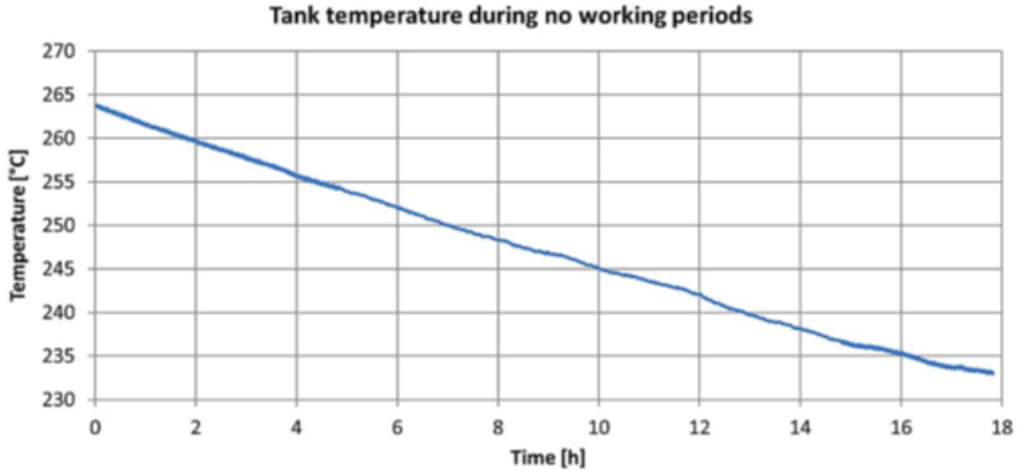

Figure 2.6 Evolution of the average salts temperature during the no-load transient.

Chapter 3

3 Development of the CFD Model

This chapter briefly describes the CFD model of the prototype storage tank installed at ENEA, which was developed as part of a previous MSc thesis work by I. Pellegrino [25].

The CFD model is capable of *solving numerically* the (partial differential) dynamic mass, momentum and energy balance equations for the fluid regions that means reproducing properly the fluid flow and the heat transfer in the salts and air regions. In addition, the CFD model solves the dynamic energy conservation equation for solids and the heat transfer at the interfaces. These physical laws are transformed into algebraic equations by subdividing the domain into a finite number of smaller *control volumes* (CVs), while the physical time is discretised in a finite number of time steps. This is a fundamental aspect in the development of a CFD model since a satisfactory trade-off between the accuracy and the computational cost, which both increase with the number of the cells in the mesh, has to be identified by means of a dedicated mesh independence study.

The model was developed using the commercial software *STAR-CCM+* with the aim of reproducing the charge and discharge transients measured during the experimental campaign. The flow field were solved by the turbulence model $k-\omega$ *SST* due to its capability of effectively dealing with both near-wall and fully turbulent regions [26], taking into account the contribution of the *gravity*, that is

fundamental for determining the buoyancy forces in the salts region. Finally, an implicit time scheme was chosen.

3.1 Domain and Boundary Condition

The benefits of CFD analysis are very high, allowing experiments to be reproduced with a high degree of *accuracy* at *lower cost*. The main drawback is the *high computational cost* of solving models, which depends, among other parameters, on the number of algebraic equations that have to be solved for each CV. A possible optimisation to reduce the number of CVs is to exploit the *symmetries* in the geometry and in the heat. As suggested in literature [27], a good solution, also valid for the thermocline TES considered here, is the use of a *2D axisymmetric domain*, which ensures an acceptable accuracy while keeping a reasonable computational cost.

This procedure was applied after some minor simplifications on accessory components. The effects of thermal bridges caused by neglected components were taken into account by calibrating the thermal resistance of the tank insulation. The impeller was considered as a static element only, excluding the blade profile in the domain (**Figure 3.1**).

Moving to the *boundary conditions* (BCs), the internal flow of the diathermic oil is not included in the computational domain. This choice allows a strong reduction in the number of cells by applying the experimental thermal load as a *heat source* to the heat exchangers wall.

A Robin BC is imposed on the external surface of the tank considering the *ambient temperature* and the *convective heat transfer coefficient* both constant and uniform. As reference data, the average temperature in Rome for each test day was retrieved from an online meteorological archive [25], while the wind speed, from which the heat transfer coefficient was calculated by appropriate correlations [28], was arbitrarily set at 7 m/s. A sensitivity analysis was

conducted on both the ambient temperature and the wind speed, which proved that their influence on the thermal losses is almost negligible.

Finally, the boundary condition corresponding with the *aperture* on the top of the tank was set as pressure outlet with ambient temperature and ambient pressure.

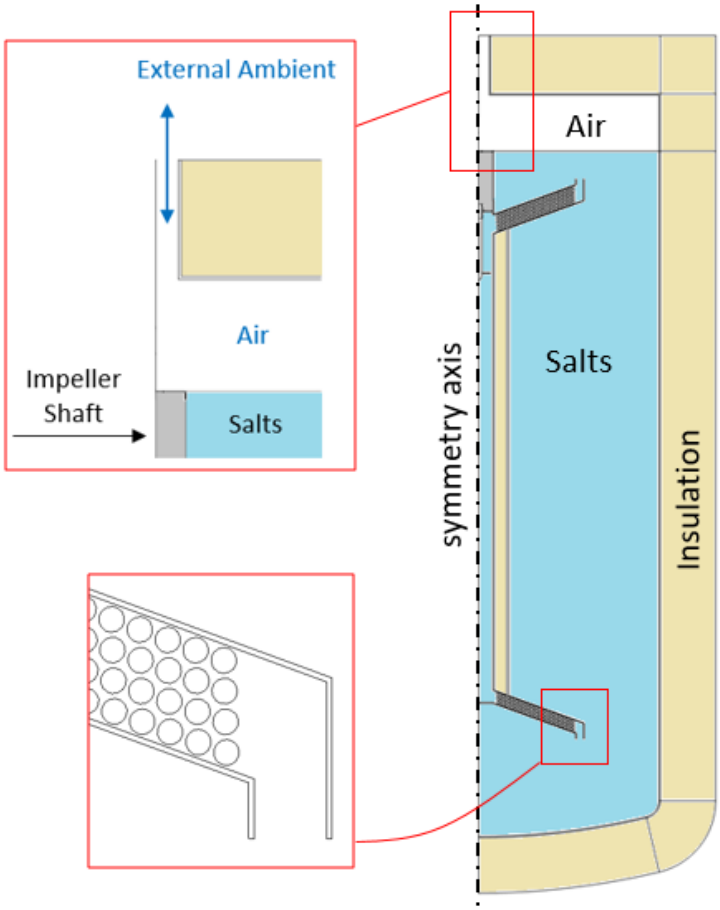

Figure 3.1 Axisymmetric 2D computational domain.

3.2 Computational Mesh

The complexity of the geometry has led to the choice of a *polygonal mesh* which, although more computationally expensive, guarantees a balanced and efficient solution (see **Figure 3.2**). The mesh has been left coarser in solid regions, where only the thermal conduction is solved, and has been refined in

the fluid regions, in which all the conservation equations are solved. The wall-fluid interfaces have been treated with 3 prism layers with a total thickness of 0.35 mm in order to guarantee a very accurate solution of the temperature and the velocity gradients.

The *all y+ wall treatment* model has been applied, which allows solving the wall gradients both in the case of $y+ \approx 1$ and in the case of high $y+$ (> 30). In the specific case it has been checked that the y+ is always equal or lower than 1.

Finally, a cell number of 10^5 was considered sufficient to guarantee the independence of the results from the calculation grid.

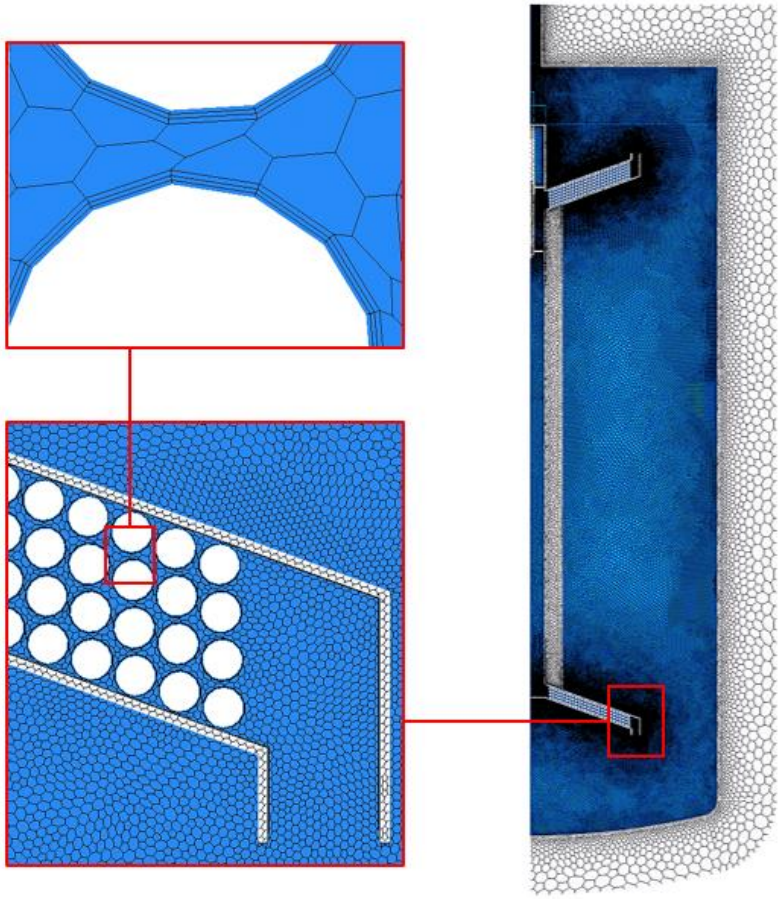

Figure 3.2 Mesh with detail of the charge heat exchanger region [25].

Similarly, the timestep independence study was carried out providing a value of 2.5 s as the right compromise between accuracy and time consumption.

3.3 Model Validation

In this section the simulation of *real transients* is presented, comparing the results from the CFD model against the outcomes of the experimental campaign. In some cases, the simulations reproduce just a fraction of the experimental test, corresponding to the test portion in which the impeller is switched off, therefore, the initial conditions have been adapted to replicate a transient already occurring. The validation of the model required the introduction of the hypothesis that a gap exists between the channel walls and the heat exchangers, which is of 23 mm according to a dedicated parametric study. The latter explains the high mass flow rate of salts in the channel obtained from the tests. The figures below show the results of the model validation during a charge transient (**Figure 3.3** and **Figure 3.4**) and a discharge transient (**Figure 3.5** and **Figure 3.6**).

The comparison of the temperature evolution at different heights within the thermocline during the charge transient highlights that the temperature rises of the CFD model lags slightly behind the measured values, but overall there is *good agreement* for each thermocouple. A good match between the computed and the experimental results is obtained at the end of the transient, looking at the salts temperature distribution along the vertical direction.

Supervisors: Prof. Roberto Zanino - Dr. Mattia Cagnoli
Candidate: RICCARDO SISTI

3. Development of the CFD model

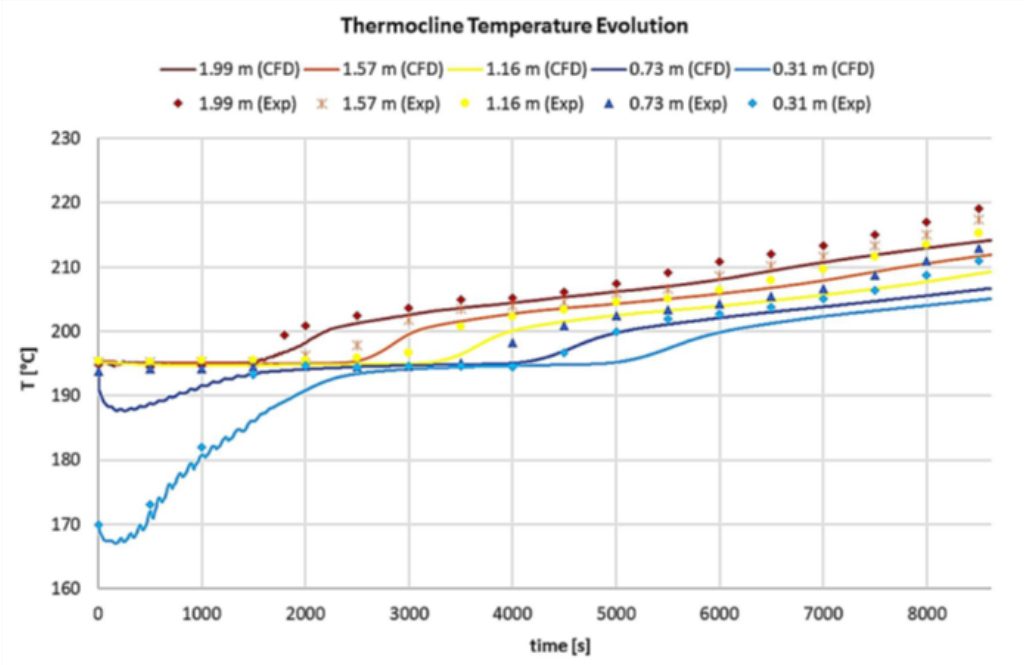

Figure 3.3 Temperature evolution at different heights: CFD and experimental comparison for the charge test 2 [25].

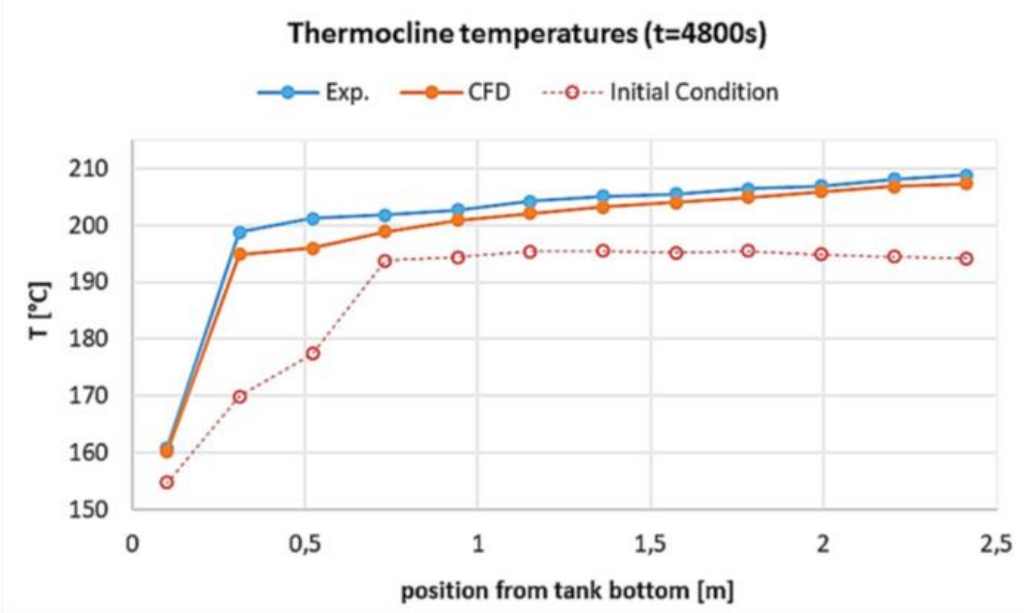

Figure 3.4 Thermocline temperatures after 4800 s of transient for the charge test 2 [25].

Similar considerations are made about a discharge transient, where the CFD evolution is again slower with respect to the experimental one, suggesting that

the experimental mass flowrate in discharge phases is still slightly bigger than the one reproduced in the CFD simulation.

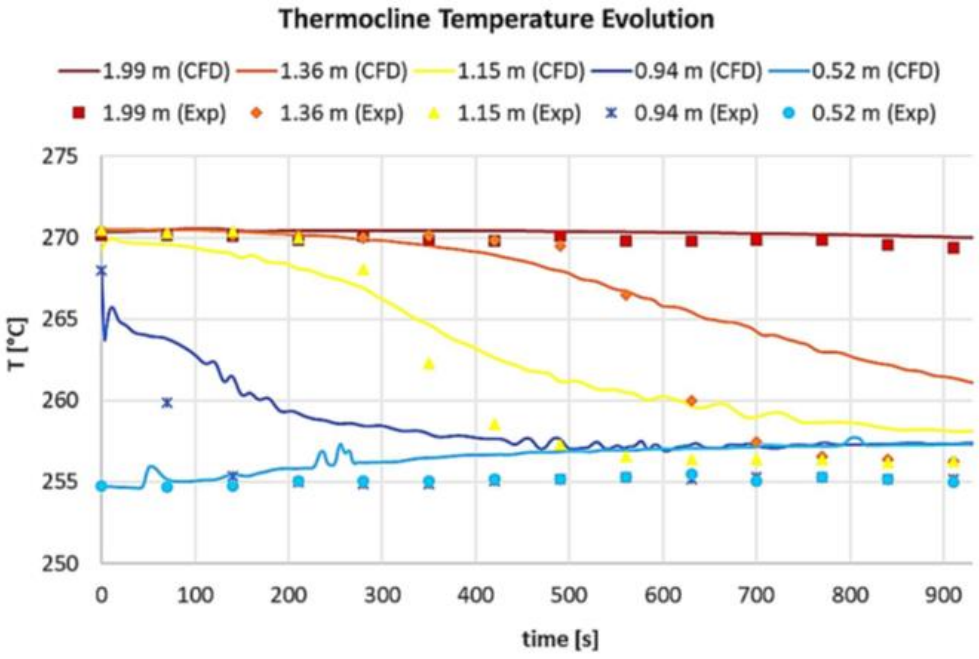

Figure 3.5 Temperature evolution at different heights: CFD and experimental comparison for the discharge test 4 [25].

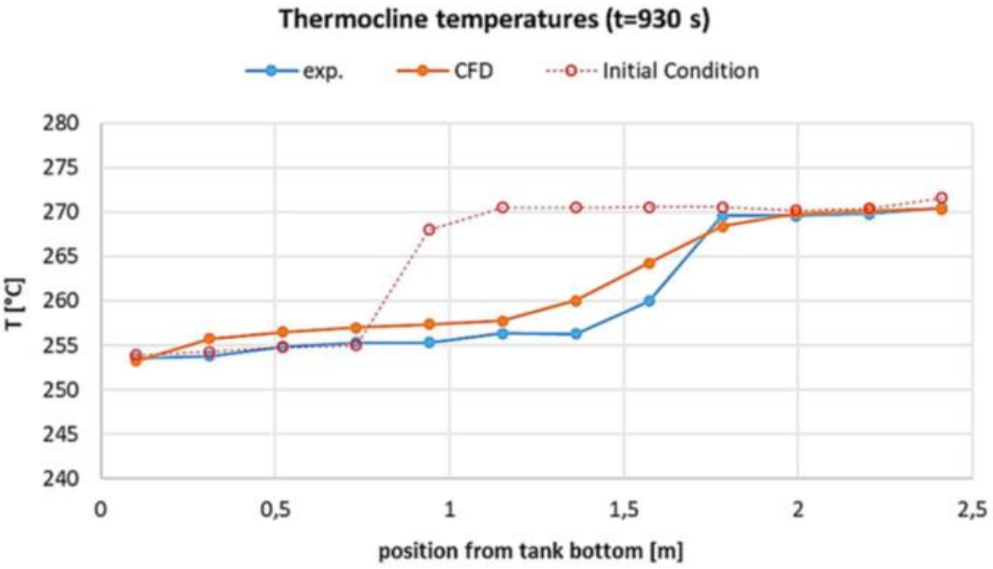

Figure 3.6 Thermocline temperatures after a transient of 930 s for the discharge test 4 [25].

Chapter 4

4 Integration of the PCM

This thesis work, carried out in close collaboration with the ENEA center of Casaccia (Rome), is focused on the *optimization of the thermal performance* of the thermocline storage system. In particular, the effect on the thermal performance due to the introduction of *phase change material* (PCM) inside the tank has been investigated through a CFD model capable to reproduce the evolution of the charge transient. The optimization of the shape and size of these inserts is also presented in this thesis.

4.1 PCM Selection

The phase change process of a material implies the release or absorption of latent heat. Phase change materials (PCMs) are exploited to store thermal energy, they have the advantage over sensible storage media of a *large heat storage density* and of a *constant charging/discharging temperature*. The main characteristics that a PCM has to satisfy are listed below:

- A melting temperature in the required operating range.
- Melt congruently with minimum sub-cooling
- Chemically stable
- Low cost
- Non-toxic and non-corrosive.

PCMs can be classified in three main group according to the *temperature range* in which the phase change occurs:

- Low-temperature PCM, where the phase change occurs below 15°C. Typical applications are cold storage for air conditioning and refrigeration.
- Medium temperature PCM (phase change temperature between 15°C and 90°C). These are the most common because they are used in the solar-driven heating systems for buildings and in the cooling of electronic devices.
- High-temperature PMCs (above 90°C) used in industrial applications, solar power plants and aerospace applications.

The **Figure 4.1** shows a more specific classification of material groups with the typical temperature range and enthalpy of fusion.

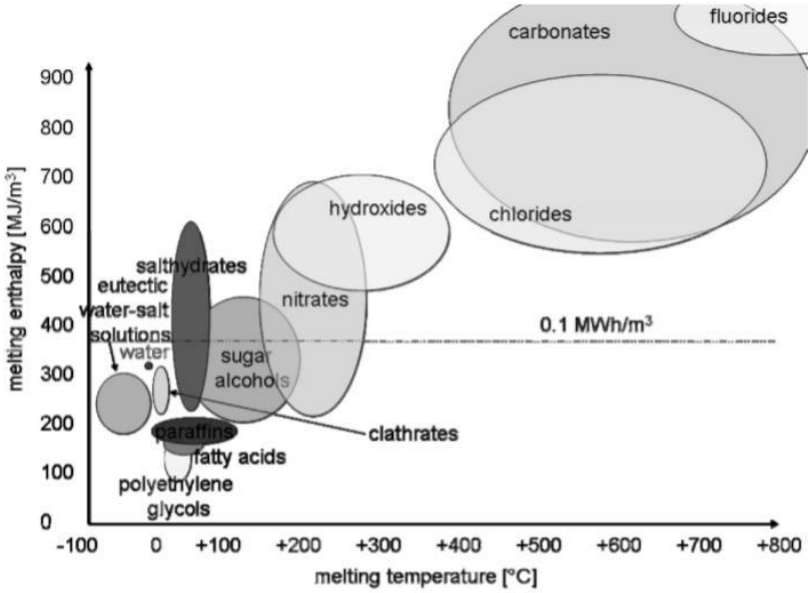

Figure 4.1 Classification according to the temperature range in which the phase change occurs [29].

Another classification of PCMs is based on the *chemical composition, which* is presented in **Figure 4.2.**

Supervisors:
Prof. Roberto Zanino - Dr. Mattia Cagnoli
Candidate:
RICCARDO SISTI

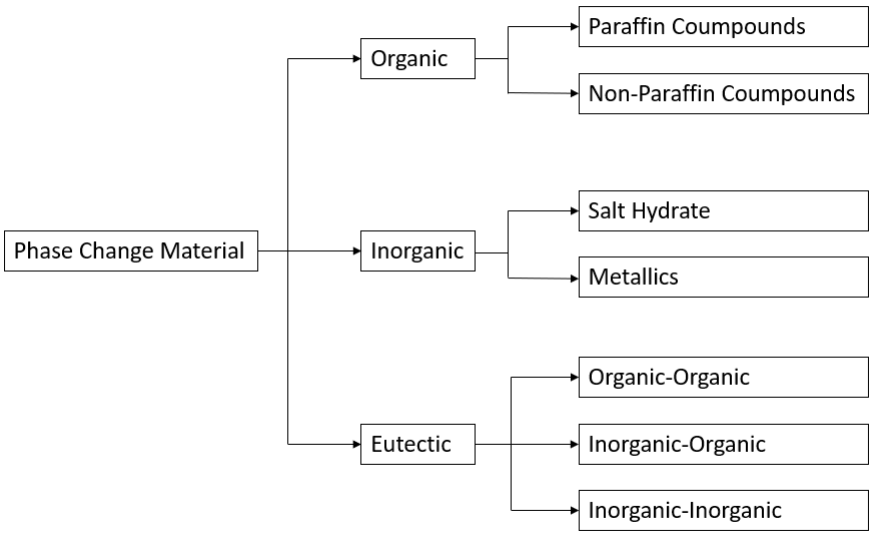

Figure 4.2 PCMs classification based on chemical composition.

Organic PCM compounds such as paraffin wax and fatty acids are inexpensive, combustible and available in large quantities. When paraffin reaches melting points, an allotropic modification takes place that makes the material being soft and plastic. They have the advantage of freezing without super-cooling (i.e. process of lowering the temperature of a liquid below its freezing point without it become a solid) and due to their large temperature range and their various forms of structure, paraffin is typically adopted for residential heating [30].

Fatty acids have similar melting ranges, heat of fusion values and application to organic paraffin substances but the cost of this material is approximately 2–2.5 times greater.

Inorganic PCMs are generally hydrated salt materials that have been extensively studied as materials for storing latent heat. The material is an inorganic compound having a high density of volumetric latent heat.

Hydrated salts are often combined with additives in order to improve the performance and delay the degradation of the PCM to prevent the material from undercooling. The main disadvantage is the corrosion of metallic materials.

Hydrated salts have melting points in a range between 0°C and 120°C [30], which makes these salts suitable for numerous thermal storage applications. Without the presence of water, the salts reach much higher melting temperatures, making them suitable for high-temperature solar power systems.

Molecular alloy PCMs (MAPCMs) are excellent materials for thermal protection and for thermal energy storage (TES). Of special interest is the fact that, by making alloys of molecular materials, the range of melting can be adjusted over a range of temperatures ensuring large latent heat and high thermal conductivity [30]. MAPCMs could be used in high temperature scenarios, have not yet been seriously considered for PCM technology because of weight penalties.

As previously mentioned, the selection of a medium for a specific application depends on the melting temperature, which must be *compatible with the thermal levels of the user* [31]. In this thesis, the end user is the power block consisting of an ORC cycle with a minimum operating temperature constraint of 260°C. The maximum temperature stored by the thermal storage system is of 285°C-290°C, which is closely related to the maximum temperature of the solar field. The choice of the phase change material to be integrated in the thermocline has been made by considering a list of materials (**Table 4.1**) selected and reviewed by ENEA. In addition to the data in the table, other parameters have been considered such as thermal capacity, thermal and chemical stability, safety, environmental compatibility, complete reversibility in loading/unloading cycles, cost, availability and recyclability [31]. The final choice fell on sodium nitrite (NaNO2), as it was the only one with the appropriate phase change temperature.

Supervisors: Prof. Roberto Zanino - Dr. Mattia Cagnoli
Candidate: RICCARDO SISTI

Table 4.1 Thermo-Physical properties of salts with medium melting temperatures (200-350°C)

Material	Density [kg/m^3]		T. melting [°C]		Spec. Heat [kJ/kg/°C]		Latent Heat [kJ/kg]	Conduct. [W/m/°C]	
wt%	Sol.	Liq.	Start	End	Sol.	Liq.		Sol.	Liq.
NaNO3/ KNO3 (54/46)	1850	1850	222	222	1.51	1.55	117	0.50	0.55
NaNO3/ KNO3 (60/40)	2008	1920	223	223	1.43	1.54	105	0.78	0.45
LiNO3	2163	1780	253	253	1.70	2.10	373	0.60	0.70
NaNO2	2109	1810	270	270	1.65	1.77	180	0.53	0.67
NaNO3	2112	1908	306	306	1.78	1.70	175	0.60	0.51
NaOH	2106	1785	318	318	2.15	2.15	165	0.92	0.92
KNO3/ KCl (95/5)	2100	2100	320	320	1.21	1.21	74		
KNO3	2106	1880	335	335	1.43	1.38	116	0.50	0.42

4.2 PCM Inserts

The choice of the geometry of the inserts filled with the PCM is of great importance since it affects the heat transfer between the PCM and surrounding fluid. The PCM conductivity is typically low, for this reason it is very important to design the inserts in such a way that they work as an efficient heat exchanger. In literature it is possible to find a wide range of solutions from the simplest double pipe heat exchangers [32] to spherical encapsulation [33].

In this thesis, in order to preserve the *axisymmetric structure* of the CFD model, it has been chosen to use toroidal tubes filled with the PCM. Additionally, this structure allows PCMs to be easily located at the desired height inside the tank. The constitutive relations for the area and the volume of a toroid are reported below.

$$A = 4\pi^2 Rr \tag{4}$$

$$V = 2\pi^2 Rr^2 \tag{5}$$

Where R is the radius of revolution and r is the external radius of the tube.

The toroidal tubes are arranged by adopting a *staggered configuration* (**Figure 4.3**) that performs better than the inline configuration for low Reynolds numbers ($Re \simeq 200$) [28].

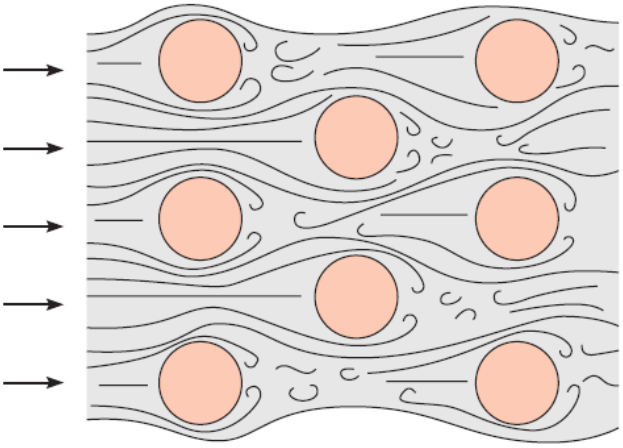

Figure 4.3 Flow conditions for staggered tubes [28].

The tube bank dimensions have been parametrically optimized to determine the most suitable configuration for the PCM inserts by evaluating the trade-off between the maximisation of the PCMs mass introduced in the tank and the heat transfer area. The introduction of the tube bank in the tank is constrained by the radius of the tank in the salts region, net of the radius of the internal channel, and the height of the thermal layer in the thermocline in which the salts temperatures are compatible with the melting temperature of the chosen PCM.

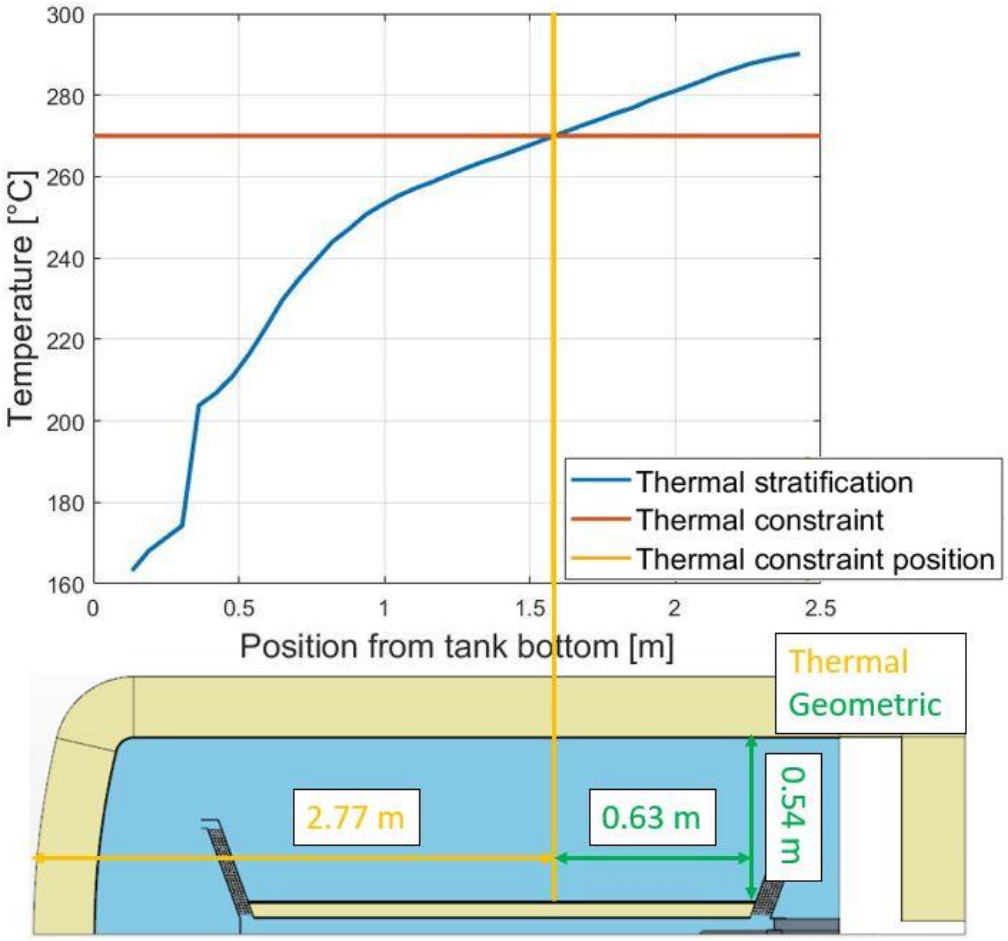

Figure 4.4 Geometric and thermal constraints: the figure above shows the thermal stratification of the salts with the indication of the position at which 270°C is reached at the end of the charging transient without PCM; the figure below shows the four constraints for the insertion of the tube bank.

In addition, a reduction coefficient of about 15%, on the maximum height of the tube bank, was considered to ensure the phase change of PCMs. **Figure 4.4** shows the selected area where to locate the inserts depending on the salts thermal stratification during the charging transient without PCM inserts. The final dimensions of the tube bank area are: 0.54 height and 0.4 width. The dimensions of the tubes considered in the parametric analysis refer to the commercial diameters (**Table 4.2**) available in the market [34] for 1mm of thickness.

Table 4.2 Commercial diameters considered in the parametric analysis.

External Diameters [mm]													
8	10	12	12.7	13	14	15	16	17.2	18	19	20	22	23	25

Regarding the distance between adjacent tubes, Wang et al. [35] presents a numerical analysis of forced-convection heat transfer in laminar, steady crossflow in banks of plain tubes in a staggered arrangement. They consider a tube bundle with 10 longitudinal rows and nominal pitch to diameter ratio parametrically varied (1.25, 1.5 and 2) for the *equilateral triangle* and the *rotated square* tube arrangements (**Figure 4.5**). The results show that:

- The lower pitch to diameter ratio, the higher the heat transfer and friction.
- The local Nusselt number and friction coefficient are higher for equilateral triangle arrangement than for the rotated square arrangement at same conditions.
- The heat transfer for the first tube in the bundle is always lower than the tubes following it (lower turbulence).

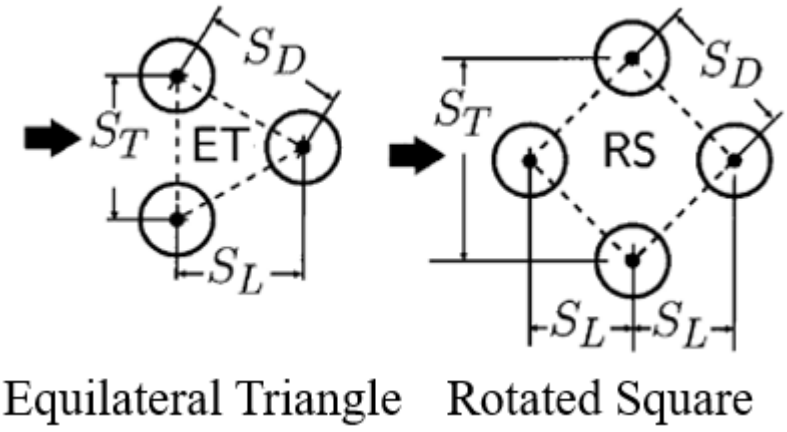

Figure 4.5 Staggered tubes arrangements [35].

For equilateral triangle:

$$S_T = S_D \tag{6}$$

$$S_L = \frac{\sqrt{3}}{2} S_D \tag{7}$$

For rotated square:

$$S_T = \sqrt{2} S_D \tag{8}$$

$$S_L = \frac{\sqrt{2}}{2} S_D \tag{9}$$

The results presented in [35] show that the equilateral triangle configuration provides a better heat transfer. The parametric optimisation has been carried out by evaluating the three possible configurations for the nominal pitch to diameter ratio seen previously. A graphical representation of the configuration selected is given in **Figure 4.6**.

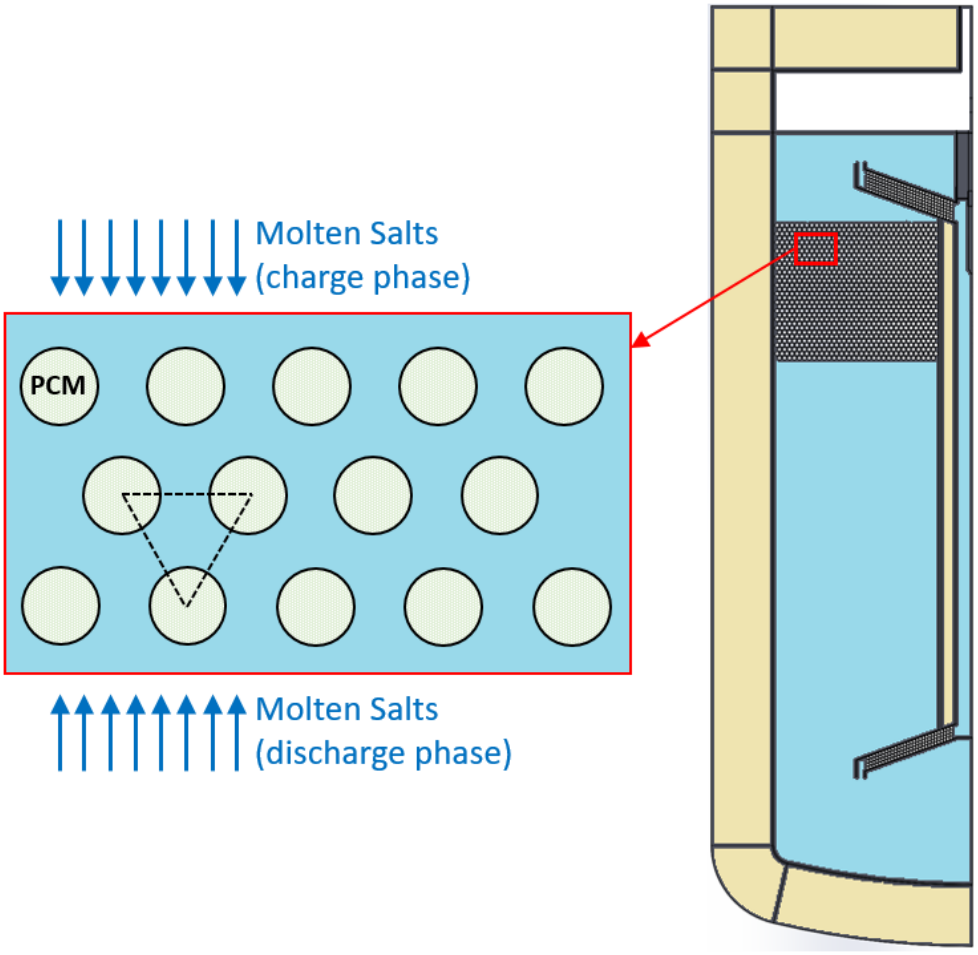

Figure 4.6 Section of the thermocline storage tank with the phase change material inserts represented by a tube bank consisting of toroidal tubes with staggered rows (equilateral triangle arrangement). The figure shows the direction of the flow of salts in the charging and discharging phase.

The equations used to define the quantities of toroidal tubes to be inserted inside the tank as a function of the pitch and external diameter are presented below. Number of columns for odd rows:

$$n_{c,o} = \frac{R - 2(pt - 1)D_{ext} - D_{ext}}{pt * D_{ext}} + 1 \tag{10}$$

Number of columns for even rows:

$$n_{c,e} = n_{c,o} - 1 \tag{11}$$

Supervisors:
Prof. Roberto Zanino - Dr. Mattia Cagnoli
Candidate:
RICCARDO SISTI

Number of rows:

$$n_r = \frac{H}{\frac{\sqrt{3}}{2} pt * D_{ext}} \tag{12}$$

Where R is the radius of the tank, net of the radius of the channel (0.54 m), H is the height of the thermocline that satisfies the constraint of the PCM melting temperature (0.4 m), pt is the pitch to diameter ratio and D_{ext} is the external diameter of the tubes.

In **Figure 4.7**, the final results of the optimization are presented: they refer to the pitch to diameter ratio equal to 1.25. This configuration is the one that has been implemented in the model, allowing the volume of PCM to be maximised. It is possible to find the other results in the **Appendix A.**

The graph shows that, for a diameter of 13 mm, the volume of the PCM introduced has a *local maximum, while the heat transfer area is still relatively high. For this reason, a diameter of 13 mm has been finally adopted in this study*. In **Figure 4.6** the final geometry is reported, it consists of *910 toroidal tubes* divided as follows: 14 odd rows of 33 tubes and 14 even rows of 32 tubes.

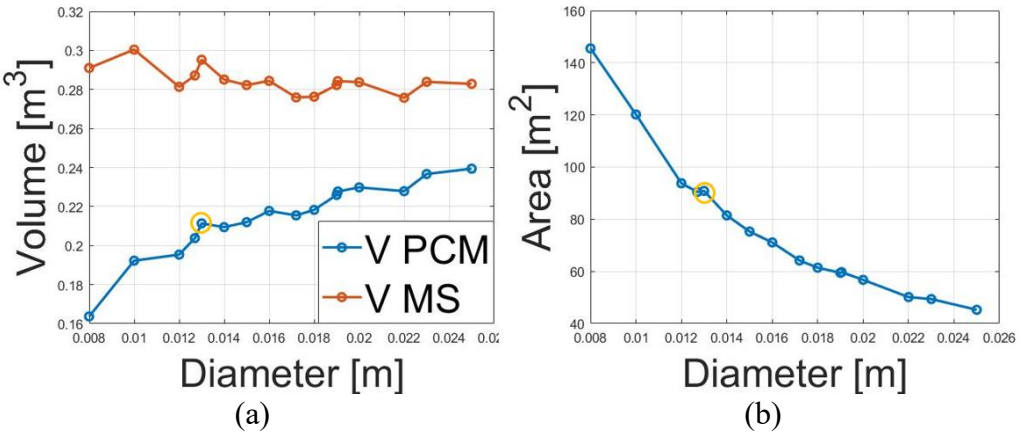

(a) (b)

Figure 4.7 (a) Introduced volume of PCM and (b) Heat exchange area as a function of the external diameter of the tubes.

Supervisors:
Prof. Roberto Zanino - Dr. Mattia Cagnoli
Candidate:
RICCARDO SISTI

The **Table 4.3** summarises in percentage terms the volume of salts to be replaced by phase change inserts.

Table 4.3 Percentage Change in HSM Volume After Introduction of PCM Inserts.

Volume	[%]
$V_{MS\ Removed}/V_{Total}$	11.2
$V_{PCM\ Introduce}/V_{Total}$	8.0
$V_{Cover\ Introduce}/V_{Total}$	3.2

4.3 Modelling of the phase change physics

In this chapter, the development of the thermocline as a whole is set aside to deal specifically with the physics of phase change. The methodology applied was to reproduce studies proposed in the literature, which consider *basic geometries* with *simplified boundary conditions* and PCM similar to that selected in this thesis. First, a fully CFD approach has been tried, with not satisfactory results; therefore, an ad-hoc lumped parameter model has been developed for reproducing the phase change physics.

4.3.1 CFD Approach

According to the *STAR-CCM+* user guide [36], the phase change can be simulated by using the *Volume of Fluid* (VOF) model that is a *multiphase model* based on the *Eulerian approach*. The VOF model is suited for simulating flows of several immiscible fluids on numerical grid capable of resolving the interface between the phases of the mixture. In the cases of immiscible fluids, free surfaces and phase contact time, there is no need for extra modelling of inter-phase interaction, and the model assumption that all phases share velocity, pressure, and temperature fields becomes a discretization error. Due to its numerical efficiency, the model is suited for simulations of flows where each phase occupies a large region of the computational domain, with a relatively small total contact area between phases. A good example of this type of flow is sloshing

flow in a tank filled by fluid, where the free surface always remains smooth. If the tank movement becomes pronounced, the formation of breaking waves, large numbers of air bubbles in the fluid and fluid droplets in the air can be detected.

The VOF model requires a fine mesh to work properly. The spatial distribution of each phase at a given time is defined in terms of a variable that is called the volume fraction:

$$\alpha_i = \frac{V_i}{V} \tag{13}$$

Where V_i is the volume of the phase i in the cell and V is the total volume of the cell. A method for calculating such distributions is to solve a transport equation for the phase volume fraction; *STAR-CCM+* uses the *Segregated Flow model*. In addition, the VOF model should be integrated by the *Melting-Solidification model* that is based on an enthalpy formulation to determine the distribution of the solid portion of the liquid-solid phase according to the equation below

$$h_{1s}^* = h_{1s} + (1 - \alpha_s^*) h_{fusion} \tag{14}$$

Where h_{1s}^* is the total enthalpy during phase change of the liquid-solid state, h_{fusion} is the latent heat, h_{1s} is the sensible enthalpy and α_s^* is the relative solid volume fraction (see Eq. 15). The last term is a function of the temperature, it is defined as the portion of the volume of the liquid-solid phase that is in the solid state. If melting and solidification take place at one temperature, a small temperature interval of 0.002 K is introduced automatically together with the assumption of a linear solidification path, otherwise, the temperature range can be set manually.

$$\alpha_s^* = f(T^*) \begin{cases} 1 & \rightarrow T^* < 0 \\ 0 \rightarrow 0 & < T^* < 1 \\ 0 & \rightarrow T^* > 1 \end{cases} \tag{15}$$

Supervisors: Prof. Roberto Zanino - Dr. Mattia Cagnoli
Candidate: RICCARDO SISTI

Where $f(T^*)$ is called the fraction of the solid curve (in this thesis, a linear dependency was assumed between α_s^* and T*) and T* is defined as:

$$T^* = \frac{T - T_{solidus}}{T_{liquidus} - T_{solidus}} \tag{16}$$

Where T is the current temperature of the PCM, $T_{solidus}$ is the temperature at which the melting starts and $T_{liquidus}$ is the temperature at which the melting ends.

The *Melting-Solidification* model that is implemented in *STAR-CCM+* does not track the liquid-solid interface explicitly and it simulates only the effect of phase change on the energy equation (i.e. it does not modify the momentum equations). A further model is required to account for the change in the material properties from liquid to solid state. The most suitable for this purpose is the *Mushy Zone Permeability* model, which behaves as follows: when the solid volume fraction increases above a critical solid volume fraction, a mushy zone permeated with dendrites is formed. The flow resistance in a mushy zone is modelled as an *isotropic porous medium* and, from a numerical point of view, it adds a source term (Si) to the momentum equation:

$$S_i = -A(\gamma)u_i \tag{17}$$

Where u_i is the velocity, while (γ) is the "porosity function" defined by Brent et al. [37] with the goal of "mimic" the Carman-Kozeny equation for flow in porous media:

$$A(\gamma) = \frac{C(1-\gamma)^2}{\gamma^3 + \epsilon} \tag{18}$$

Supervisors: Prof. Roberto Zanino - Dr. Mattia Cagnoli
Candidate: RICCARDO SISTI

The constant C is the mushy zone constant and it controls the degree of penetration of the convection field into the mushy region, γ is the liquid fraction and ϵ is a computational constant introduced to avoid division by zero.

Benchmark against the literature

The reference used for the benchmark is the one of Assis et al. [38], who conducted a numerical study of *melting in a spherical shell*. The PCM used was *paraffin wax*, which despite having melting temperatures far from NaNO2, has comparable physical properties (see **Table 4.4**):

Table 4.4 Paraffin wax physical properties.

Material	Density [kg/m^3]		T. melting [°C]		Spec. Heat [kJ/kg/°C]		Latent Heat [kJ/kg]	Conduct. [W/m/°C]	
	Sol.	Liq.	Start	End	Sol.	Liq.		Sol.	Liq.
Paraffin Wax	870	760	28	30	2.4	1.8	179	0.24	0.15

The spherical shell has an internal diameter of 80 mm and a thickness of 1 mm; it is 85% paraffin-filled and 15% air-filled at the initial state with an opening at the top to allow air to escape during volumetric expansion. The domain is reduced by a 2D axisymmetric approximation in order to reduce the computational cost (**Figure 4.8**).

The assumption introduced in the work of Assis are listed below

- Constant physical properties for solid and liquid phase during the melting transition.
- Solid and liquid phases are homogeneous.
- Solid and liquid phase are isotropic.
- Melting process is axisymmetric.

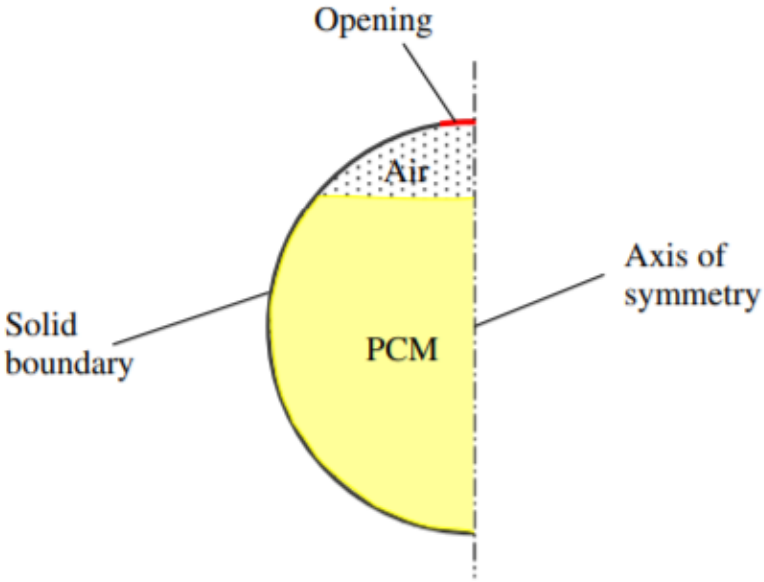

Figure 4.8 Computational domain [38].

The initial temperature of the whole system is 23 °C, while the temperature of the sphere wall is imposed as a boundary condition, it is 10 °C higher than the PCM melting temperature. The mesh consists of 3520 cells, which are enough to provide mesh independent results, and the time step is equal to 0.002 s. The physics used is the same as the one discussed in the previous chapter (Volume of Fluid, Enthalpy Formulation and Carman–Kozeny equation) setting the porous viscous resistance (i.e. mushy zone constant) to $10^5\ kg/m^3 s$.

The simulation was set up with the same parameters as the reference study. The computed fraction of liquid volume over the time has been compared with those obtained by Assis (**Figure 4.9**).

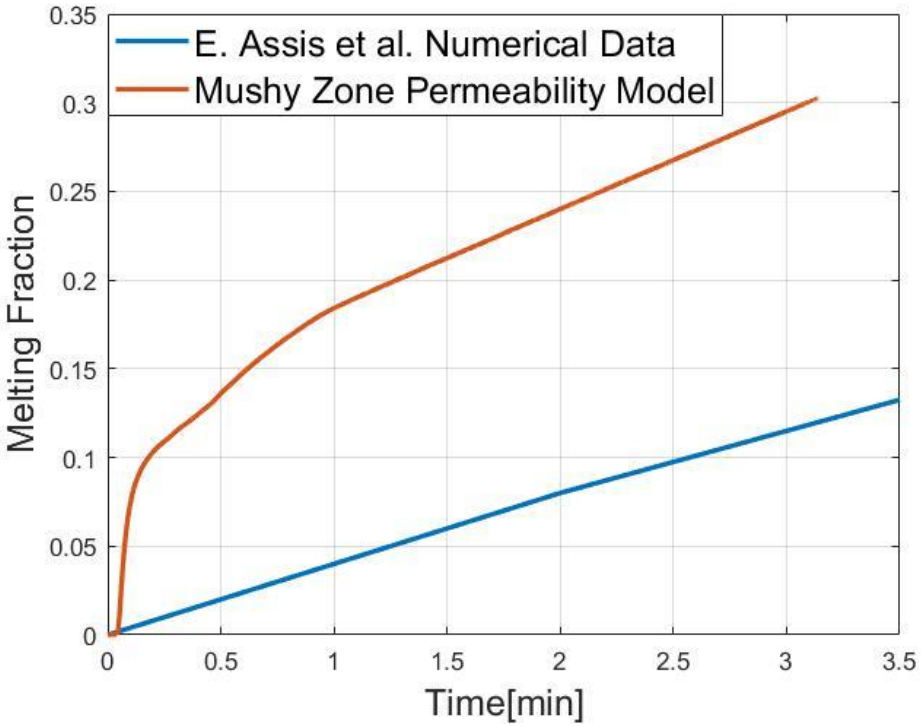

Figure 4.9 Comparison between E. Assis numerical data and CFD mushy zone permeability model.

After just three minutes of physical time, the change in volume fraction exceeds 15% and it can be concluded that the comparison is not satisfactory.

The cause of this mismatch is likely due to the STAR-CCM+ models implemented for the phase change simulation, which are not suited for this specific case of study. This statement is supported by the fact that also the STAR-CCM+ assistance, which has been contacted asking for support, was not able to provide an effective solution to that problem, i.e. to suggest how to set the models to reproduce the case of study. In addition, it has to be highlighted that the computational cost of the CFD model is huge, requiring several days of simulation just for this test case. The calculations were carried out on a machine equipped with the Intel Xeon E5-2630 v3 (2.4 GHz) in which only four cores were used and 128 GB of RAM.

For these reasons, a new approach has been tried, based on a lumped parameter model, which is being presented in the next section.

4.3.2 Lumped Parameters Approach

A 0D model has been developed to reproduce the physics of the phase change. The 0D approximation is useful to simplify otherwise the numerical representation of complex differential heat equations. In a 0D model, the spatial distribution of the temperature is not considered, the temperature inside the object is assumed to be uniform, although this uniform temperature changes over time.

Therefore, it follows that phenomena related to the density variation (i.e. buoyancy forces and thermal expansion) are not taken into account. The analysis assumes that at each time the control volume is in *thermodynamic equilibrium*, which implies the containment, within the control volume, of a homogeneous mixture in equilibrium at each instant. Phenomena such as temperature gradients, pressure waves, non-equilibrium compositions, vaporization and mixing are therefore ignored.

The 0D model solves the dynamic energy conservation equation applied to the phase change material (Eq. 19). The heat accumulated in the metal wall of the tube is neglected as it is almost negligible, while the thermal resistance offered by the tube wall is considered.

$$M\frac{de}{dt} = q \tag{19}$$

Where M is the mass of the PCM in the tube, e indicates the specific energy in [J/kg], t is the time and q represents the heat flux in [W] exchanged between the salts and the phase change material. Depending on the phase of the PCM, the energy equation is written by means of Eq. 20 (solid), Eq. 21 (phase change) or Eq. 22 (liquid).

$$Mc_{ps}\frac{dT_{PCM}}{dt} = q \tag{20}$$

Supervisors: Prof. Roberto Zanino - Dr. Mattia Cagnoli
Candidate: RICCARDO SISTI

$$M\frac{dL}{dt} = q \tag{21}$$

$$Mc_{pl}\frac{dT_{PCM}}{dt} = q \tag{22}$$

Where, T_{PCM} is the temperature of the PCM, L is the latent heat, c_p is the specific heat, while the subscripts s, l indicate whether the quantity refers to solid or liquid, respectively.

Different heat transfer mechanisms are considered in the model and represented in **Figure 4.10**. Starting from the tube outer wall, the radial conduction in the tube is calculated and thus the heat transfer between the tube inner surface and the phase change material, which occurs by conduction or convection depending on the phase of the PCM.

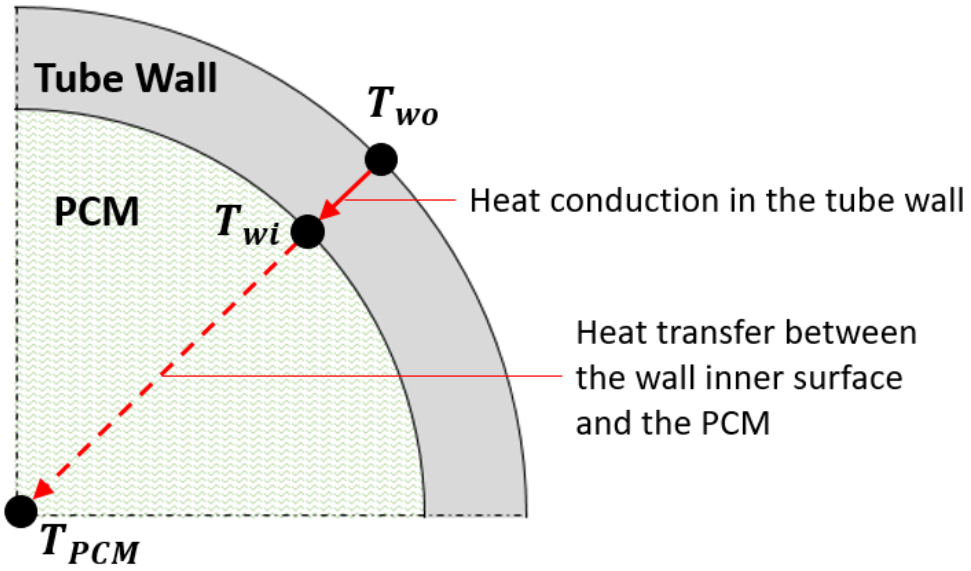

Figure 4.10 Scheme of the heat exchanges considered in the concentrated parameter model: heat exchange by radial conduction and heat exchange between internal wall and PCM as a function of the phase of the latter.

Radial conduction in the pipe is calculated as:

$$q = k_w \frac{2\pi x}{ln(D_o/D_i)}\left(T_{w,o} - T_{w,i}\right) \tag{23}$$

Where, k_w is the thermal conductivity of the AISI 316 steel wall, D is the pipe diameter, x is the length of the pipe axis and T_w is the wall temperature; subscripts o, i denote the external and internal wall surfaces respectively.

The heat transfer between the inner wall and the PCM is calculated by means of Eq. 24 (solid), Eq. 25 (phase change) or Eq. 26 (liquid).

$$q = k_s \times 2\pi x\left(T_{w,i} - T_{PCM}\right) \tag{24}$$

$$q = h_0 \times \pi D_i x\left(T_{w,i} - T_m\right) \tag{25}$$

$$q = h_l \times \pi D_i x\left(T_{w,i} - T_{PCM}\right) \tag{26}$$

Where, k_s is the thermal conductivity of the PCM in the solid phase, h_l and h_0 are the convective heat transfer coefficient for the liquid and for the phase transition, respectively, and T_m is the melting temperature.

The heat transfer coefficient for the liquid phase is derived from the correlation proposed by D.R. Oliver [39] who investigated the effect of natural convection on viscous-flow heat transfer in horizontal tubes.

$$Nu = 0.35(\mathrm{Pr} * \mathrm{Gr})^{0.35} \tag{27}$$

Where the Nusselt number (Nu) is function of the Prandtl Number (Pr) and the Grashof Number (Gr).

Supervisors:
Prof. Roberto Zanino - Dr. Mattia Cagnoli
Candidate:
RICCARDO SISTI

The last term to be determined is the heat transfer coefficient for the melting process, which has been identified by reviewing the literature as follows.

Benchmark against the literature

Initially, as proposed by Mina Rouhani et al. [40], PCM diffusion was assumed to be the predominant mode of heat transfer in the liquid phase, so convective heat transfer was neglected. Unfortunately, given the low conductivity of the material under consideration, this turned out to be a too strong assumption as can be seen in **Figure 4.11** where the comparison between the 0D model and the reference from Assis et al. [38] is shown.

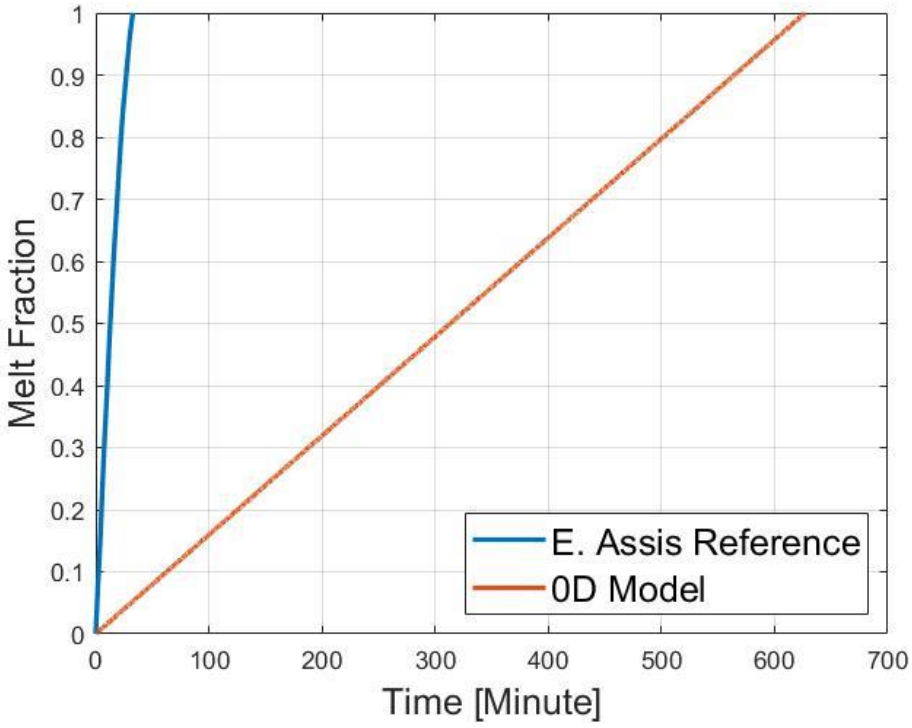

Figure 4.11 Comparison between E. Assis numerical data and conductive lumped parameters model.

These results clearly indicate that a pure conductive model is not able to correctly reproduce the phenomenon of interest. Therefore, a deeper investigation is required to identify a suitable correlation for the heat transfer during the phase change.

A detailed study of melting with natural convection in an enclosure has been performed by P. Jany et al. [41]. They identify the most basic scales and regimes

of the melting phenomenon with natural convection in a rectangular enclosure. In the proposed experiment, the solid is heated from the left side, while the right side is assumed to be adiabatic. The process is subdivided in four principal phases (see **Figure 4.12**) which cause variations in the Nusselt number curve presented in **Figure 4.13**:

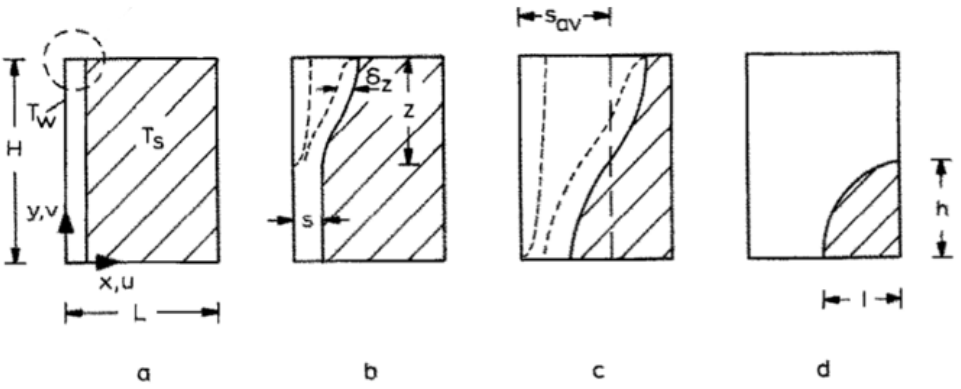

Figure 4.12 Four regime model [41].

a) At the beginning of the melting process is driven by pure conduction and depends on the liquid layer thickness. As a result, the heat transfer coefficient has a large value which means that ideally it tends to infinity.

b) Subsequently, a mixed-regime condition is established that takes the melting process from being mainly conductive to being dominated by the convection: the weak convective heat current flows vertically through the s-wide gap from the bottom end of the hot wall and is absorbed by the top end of the liquid-solid interface. The final condition is achieved when z become equal to H end; at the end of this stage, the Nu value reaches the local minimum.

c) At this point, the entire liquid zone is mostly subject to convection and the rate of heat transfer is related to the speed with which the melting front advances to the right. The Nusselt number grows until it reaches a point of relative maximum where the liquid touches the right-end wall.

d) Finally, the melting rate depends on the size of the remaining solid, which the reduction of its shape causes a close to linear decrease in the Nu number until to reach zero-solid condition.

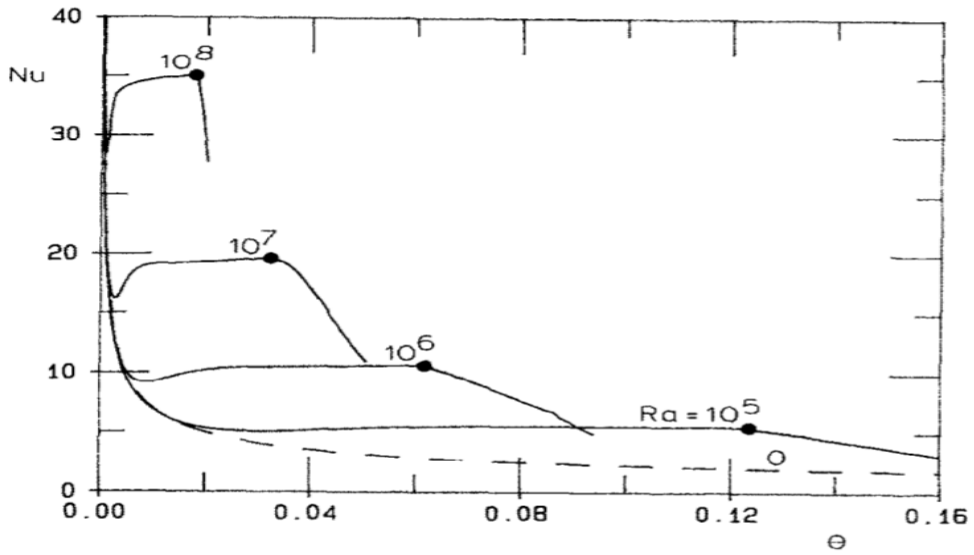

Figure 4.13 Numerical solutions for the average Nusselt number at the heated wall, as a function of time and Rayieigh number [41].

Archibold et al. [42] proposed correlations for the melting fraction and the average Nusselt number as a function of the main dimensionless parameters that characterize the problem. *Nusselt number* and the fraction of the melted material were correlated with the dimensionless Grashof number (Gr), Prandtl number (Pr), Stefan number (Ste), Fourier number (Fo), considering also, the thermal conductivity of the PCM (k_{PCM}) and the wall (k_w) ($\chi = 1 - k_{PCM}/k_w$) and the under-cooling parameter ($\zeta = 1 - T_0/T_m$), with T_0 equal to the initial temperature of the system. Archibold analysed the melting evolution of the NaNO3, which has similar properties (see **Table 4.5**) with respect to the NaNO2 considered in this thesis, in a spherical shell in different conditions.

Supervisors: Prof. Roberto Zanino - Dr. Mattia Cagnoli
Candidate: RICCARDO SISTI

Table 4.5 NaNO3 physical properties.

Material	Density [kg/m^3]		T. melting [°C]		Spec. Heat [kJ/kg/°C]	Latent Heat [kJ/kg]	Conduct. [W/m/°C]	
	Sol.	Liq.	Start	End			Sol.	Liq.
NaNO3	2130	1908	307	307	$444.53 + 2.18T$	178	0.68	0.57

Different evaluations have been carried out, each characterised by varying the geometry, the boundary and the initial conditions, as well as the material constituting the shell. The spherical shell has a thickness of 1 mm and the domain is reduced by a 2D axisymmetric approximation in order to reduce the computational cost.

The main assumption are:

- Constant physical properties for solid and liquid phase during the melting transition except for specific heat that assumes a linear distribution.
- Solid and liquid phases are homogeneous.
- Solid and liquid phase are isotropic
- Melting process is axisymmetric

The Nu and melt fraction is presented in **Figure 4.14** net of the parameter Ψ.

$$\Psi = \frac{St^{0.66}}{Gr^{0.29} Pr^{0.4} \chi^{0.72} \zeta^{0.02}} \tag{28}$$

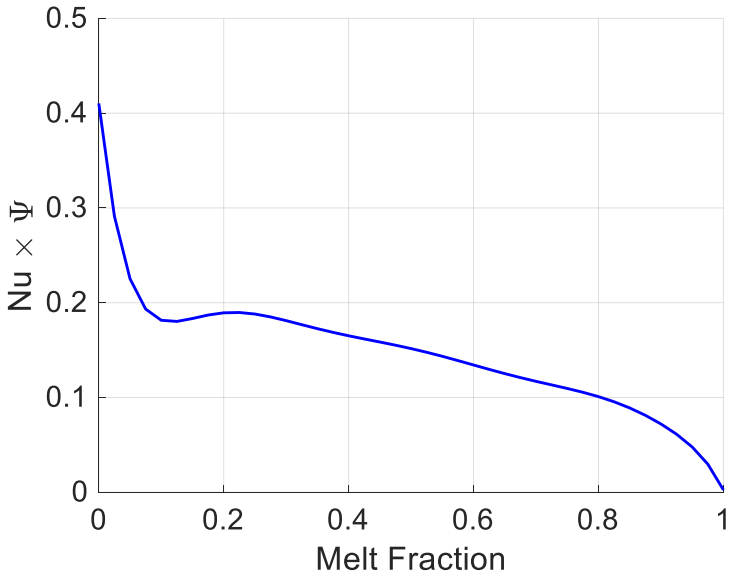

Figure 4.14 Development of the Nusselt number multiplied by the factor ψ as a function of the dimensionless Stefan, Grashof and Prandtl numbers, of the thermal conductivity of the PCM and the wall and of the undercooling parameter as a function of the melt fraction.

The lumped parameter model based on the obtained correlation has been implemented in a Matlab code using the backward Euler method. The result for the first case is presented in **Figure 4.15**; the **Appendix B** presents the other results and the characteristic data for each case study.

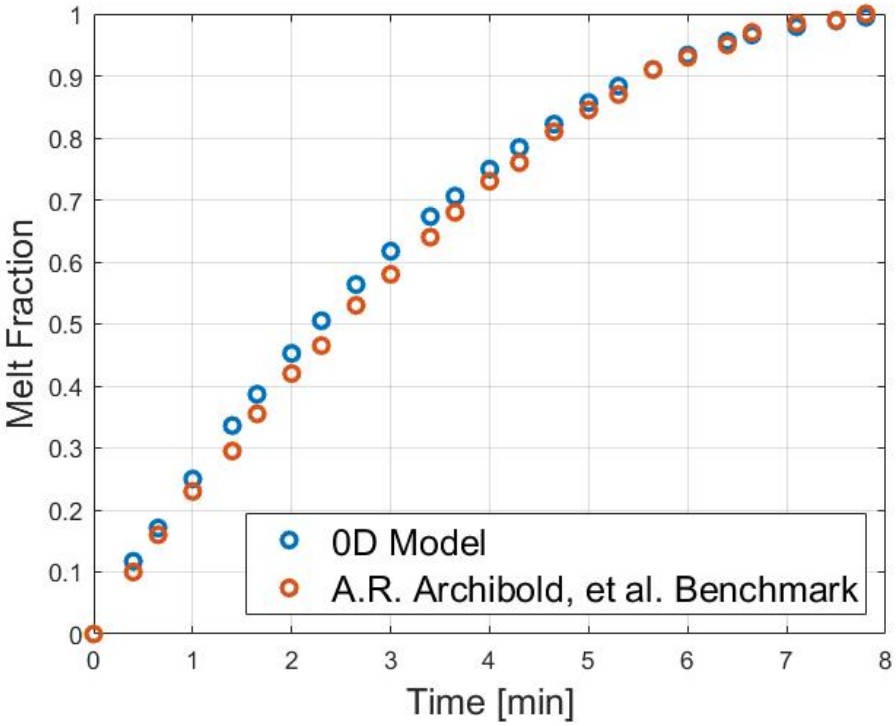

Figure 4.15 Comparison between Archibold numerical data and 0D model.

To quantify the difference between the curves in **Figure 4.15**, the coefficient of determination (R^2) and the relative error on the total time (ϵ) have been calculated. The former is given by the following equation

$$R^2 = 1 - \frac{RSS}{TSS} \tag{29}$$

Where TSS is the total sum of square dependent form the observed data (y_i) and the mean value of the observed data ($\bar{y}_i$). TSS is calculated as

$$TSS = \sum_{i=1}^{n} (y_i - \bar{y}_i)^2 \tag{30}$$

RSS is the residual sum of square of the difference between the observed data (y_i) and the data from the model ($\hat{y}_i$). RSS is calculated as

$$RSS = \sum_{i=1}^{n} (y_i - \hat{y}_i)^2 \tag{31}$$

If R^2 is equal to 1 the model predicts the experimental data perfectly, while if R^2 is equal to 0 the model predicts the experimental data no better than the mean value.

The relative error in the total time is easily defined as the relative difference between the total time required to complete the transient considering the model of Archibold and the required time using the 0D model.

$$\epsilon = \frac{\left| t_{Arch} - t_{0D,model} \right|}{t_{Arch}} 100 \tag{32}$$

The error analysis, shown in **Table 4.6**, leads to the conclusion that, as an average, R^2 is about 0.99, while the relative error on the total time is about 3.6 %. The results clearly show that the 0D model is in a quite good agreement with the results obtained by Archibold.

Supervisors: Prof. Roberto Zanino - Dr. Mattia Cagnoli
Candidate: RICCARDO SISTI

Table 4.6 Error results for each benchmark.

Case	R^2 [%]	Relative error on the total time [%]
1	0.995	4.3
2	0.998	5.6
3	0.998	1.3
4	0.997	3.1
5	0.996	4.3
6	0.988	4.1
7	0.986	5.6
8	0.975	1.7
10	0.985	1.0
11	0.98	3.4
Average	**0.990**	**3.4**

The results of this benchmark are therefore satisfactory, opening the door to the development of a model capable of integrating the representative phase change physics into the thermocline CFD model.

4.4 Thermocline CFD Model with PCM Inserts

This chapter describes the integration of the PCM inserts in the CFD model of the thermocline storage presented in **Chapter 3**. All the analyses carried out previously, to the benchmark of the melting process, are used to develop the final model that couples the *CFD model* of the thermocline storage with the PCM inserts with the *lumped parameter model* that solves the physics of the phase change.

4.4.1 Thermocline TES configuration considered in this study

The validation of the model, conducted in the previous thesis work, was obtained by introducing a by-pass above the charge HX and below the discharge HX. The by-pass reduces the thermal performance of the thermocline storage because a large share of the molten salts in the channel does not pass through the HX serpentine. For this reason, the by-pass is not considered in this optimization study, but instead the original design of the storage system is adopted.

The design operating conditions of the thermocline storage are indicated in **Figure 4.16**, which have been used as a reference in this thesis.

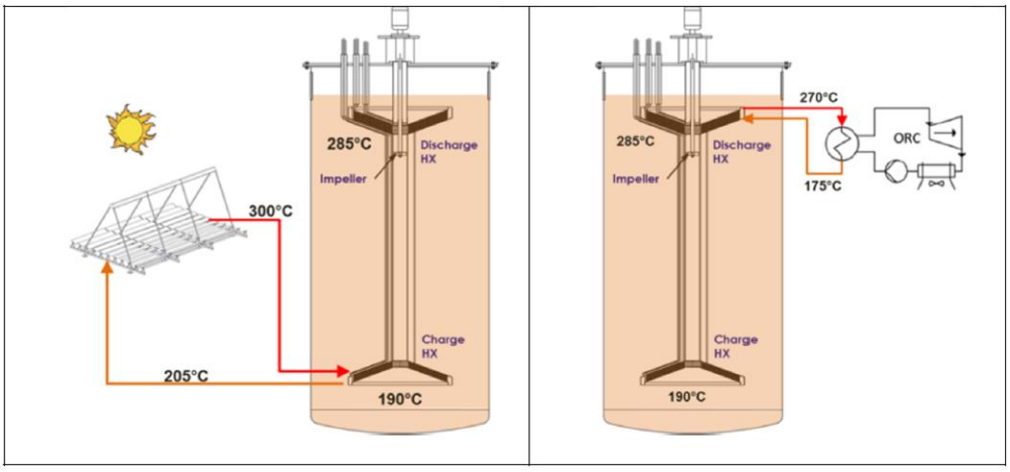

Figure 4.16 Scheme of the coupling CSP-TES-ORC [43].

As already mentioned, this thesis aims at simulating a charge transient; for this purpose, suitable initial and boundary conditions have to be introduced. The imposed initial conditions include the temperature distribution in the molten salts region, as well as the salts velocity. According to the operating conditions (**Figure 4.16**), a uniform salts temperature, equal to the oil temperature at the charge HX outlet (205 °C), has been imposed at the initial time, except for the bottom layer (below the channel) where the temperature is expected to be lower because the salts in this region are not recirculated. On the base of the experimental and numerical data, a temperature of 158 °C is assumed in the bottom layer.

Supervisors:
Prof. Roberto Zanino - Dr. Mattia Cagnoli
Candidate:
RICCARDO SISTI

In the present study, by the way, an *indirect storage system* is analysed and the maintenance of efficiency in the charge heat exchanger is a constraint imposed to respect the temperature conditions at the *solar field*. The storage is fully charged when the top layer of the molten salts reaches the design temperature of 285°C, while the layer corresponding to the inlet of the charge HX, is not lower than the design temperature of 190 °C (**Figure 4.17**).

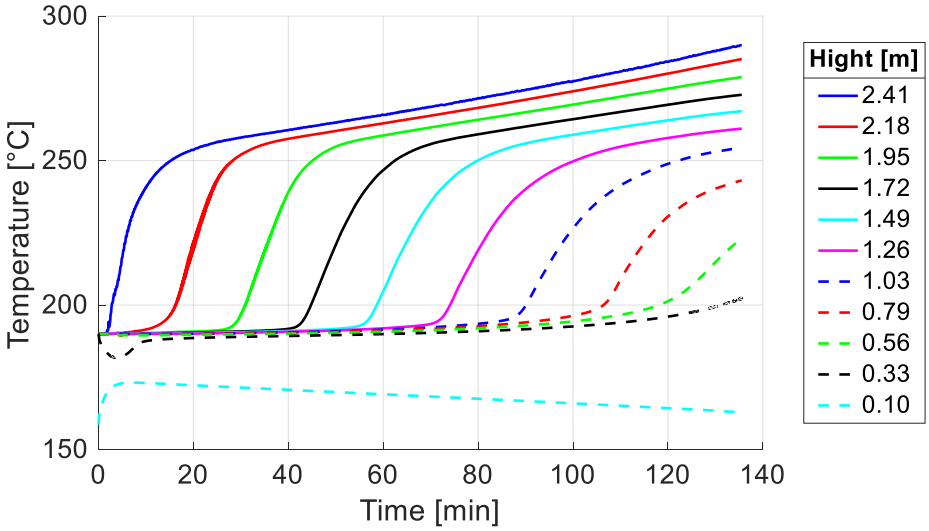

Figure 4.17 Storage system without PCM inserts: evolution of salt temperature over time during the charging transient, for different eights from the tank base (salt side).

These conditions are satisfied by imposing a heat source equal to 135 kW on the outer surface of the charge heat exchanger. The thermal (sensible) *energy stored* during the entire transient is equal to 297.76 kWh net of the energy used to reach the initial conditions.

4.4.2 CFD Model

The introduction of the tube bank substantially modifies the geometry of the thermocline, but the choice of using toroidal inserts allows the assumption of 2D-axisymmetry to be maintained. The same mesh setting and time discretization of the previous CFD model (see **Chapter 3**) are adopted here.

Thus, the *time-step* remains equal to 2.5s with 5 iterations for each time-step, while the *mesh* doubles its number of cells (from about $1x10^5$ to $2x10^5$) due to the need of solving accurately the thermal and velocity gradients at the interface between the salts and the tube bank walls (**Figure 4.18**).

The non-dimensional wall distance y+ was recalculated in the area of interest, verifying that a value of approximately 1 was respected. The boundary conditions remain unchanged, except for the introduction of a *Robin-type boundary condition* between the molten salts and the outer wall of the toroidal tubes, which allows coupling the CFD model with the lumped parameter model.

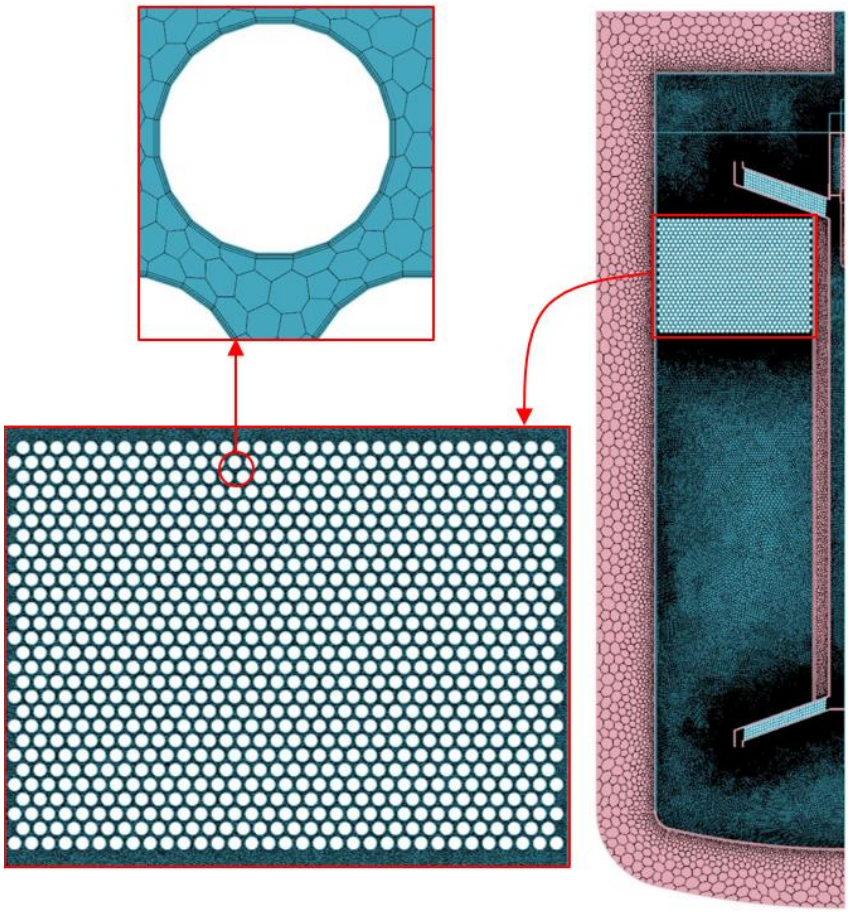

Figure 4.18 On the right calculation grid for the storage tank with PCM inserts; on the left bottom detail of the tube bank; on the left top detail of the single tube.

Supervisors:
Prof. Roberto Zanino - Dr. Mattia Cagnoli
Candidate:
RICCARDO SISTI

4.4.3 Integration of the Lumped Parameters Model

To couple the CFD model with the lumped parameter model, the latter has been developed as a *User-Code* compatible with the STAR-CCM+ software. The User-Code allows customizing the CFD code with functions written in C, C++ or Fortran [36]. User-Code takes the form of one or more user libraries each of which contains one or more user functions and a library registration function. It could be possible to use these functions to specify values on a region or on a boundary. *STAR-CCM+* has standardised its functions by defining them through a signature (i.e. arguments and output have a standardized type), and so each function of the User-Code can request arguments from *STAR-CCM+* and return a result to the simulation. The two principal categories of user functions are: User-Coded Profile and User-Coded Field Function. For the generation of a user code three files are necessary: the first one is for the definition of variables and functions, the second one is for the declaration and finally the third file contains the actual code.

The last step is done by linking these files to the "*UserFunction.lib*" library to create a dynamic library that can be loaded on the simulator. More specifically, for each time step the developed User-Code takes the salt temperature at the interface with the toroidal tubes, the time-step and the physical time and it returns the PCM temperature together with the heat transfer coefficient, these output values from the User-Code are read by STAR-CCM+ as a Robin type boundary condition. The structure of the code is presented in **Figure 4.19**: for each row of toroidal tubes, two functions (one for the temperature and one for the heat transfer coefficient) have been written to handle the inputs and to write the outputs. Subsequently the numerical calculation is computed by two additional functions which solve the energy equations for all the rows of toroidal tubes.

In order not to increase the computational cost excessively, the salts temperature is computed as the average of two consecutive rows in the tube bank; therefore, since the tube bank consists of 28 rows, 14 temperatures at salts-

tubes interface are actually calculated. This assumption is justified since the thermal gradient between two rows of tubes does not exceed 0.5°C as it is displayed by comparing the results of the thermocline simulation without PCM and the outcomes from the model with the phase change material inserts.

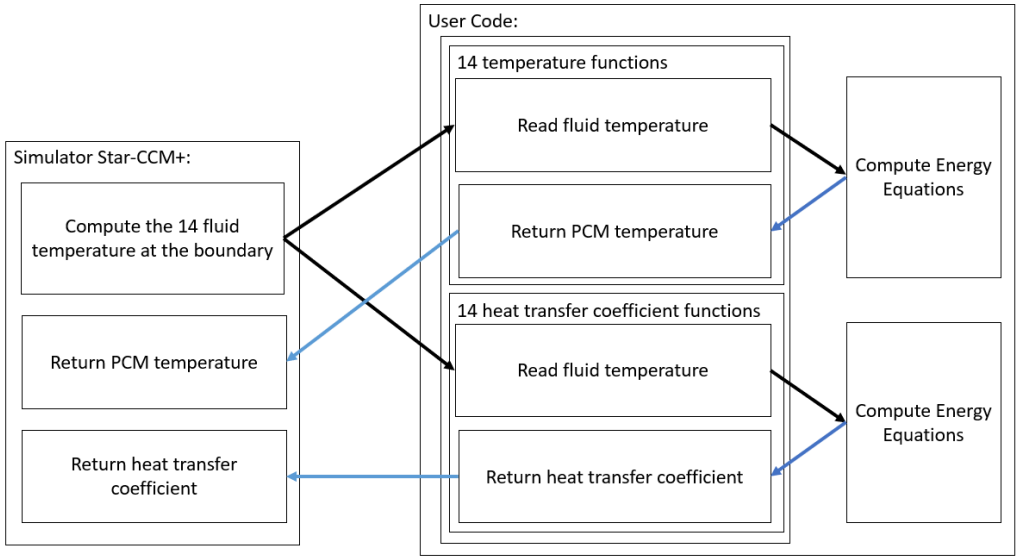

Figure 4.19 User-Code Structure for the 0D Model.

4.5 Result and Discussion

In this section, the CFD model coupled with the lumped parameter model is used to simulate the thermal fluid dynamic performance of the thermocline system during a charge transient. The purpose of the study is to verify the effect on the thermal performance of the introduction of phase change inserts in the tank. For this scope, the results are compared with those of the configuration without PCM presented.

The two systems are compared for the same amount of time equal to 135 minutes, i.e. (since the power is assigned equal to 135 kW) for the same amount of storable energy (297.76 kWh). As a first output, the calculated *temperature and velocity distribution* at the end of the transient are shown in **Figure 4.20.a.** It is possible to appreciate the thermal stratification inside the bulk of the molten salts, the role of the external insulation layers, in which a high temperature

gradient is set, protecting the molten salts from the cold external temperature and the low air inlet temperature from the opening at the top of the tank. The maximum temperature of the salts is inside the channel, at the outlet of the charge heat exchanger. In **Figure 4.20.b** it is observed the salts moving by buoyancy forces in the internal channel, from the bottom towards the top of the tank. As expected, the maximum velocity is reached inside the channel according to the conservation of mass, being the section of the channel much smaller than that of the tank.

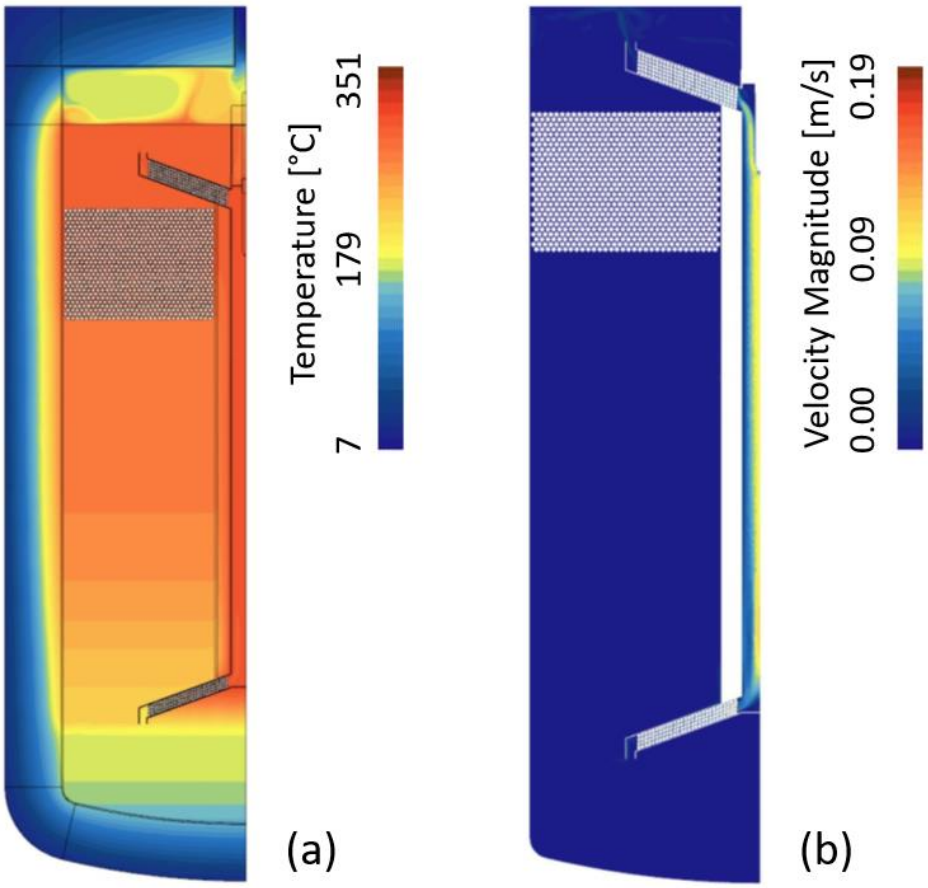

Figure 4.20 CFD model results at the end of the charge transient: (A) map of temperature distribution in the computational domain and (B) velocity distribution in the salts region.

The *time evolution of the temperature* of the phase change inserts for the different heights at which they are located within the tank is shown in **Figure**

Supervisors:
Prof. Roberto Zanino - Dr. Mattia Cagnoli
Candidate:
RICCARDO SISTI

4.21. The classic pattern of a material experiencing the phase change can be noticed, characterised by a time interval in which the heat is absorbed at constant (melting) temperature, in this case 270°C. At the end of the transient, the phase change is completed in all the rows of the tube bank.

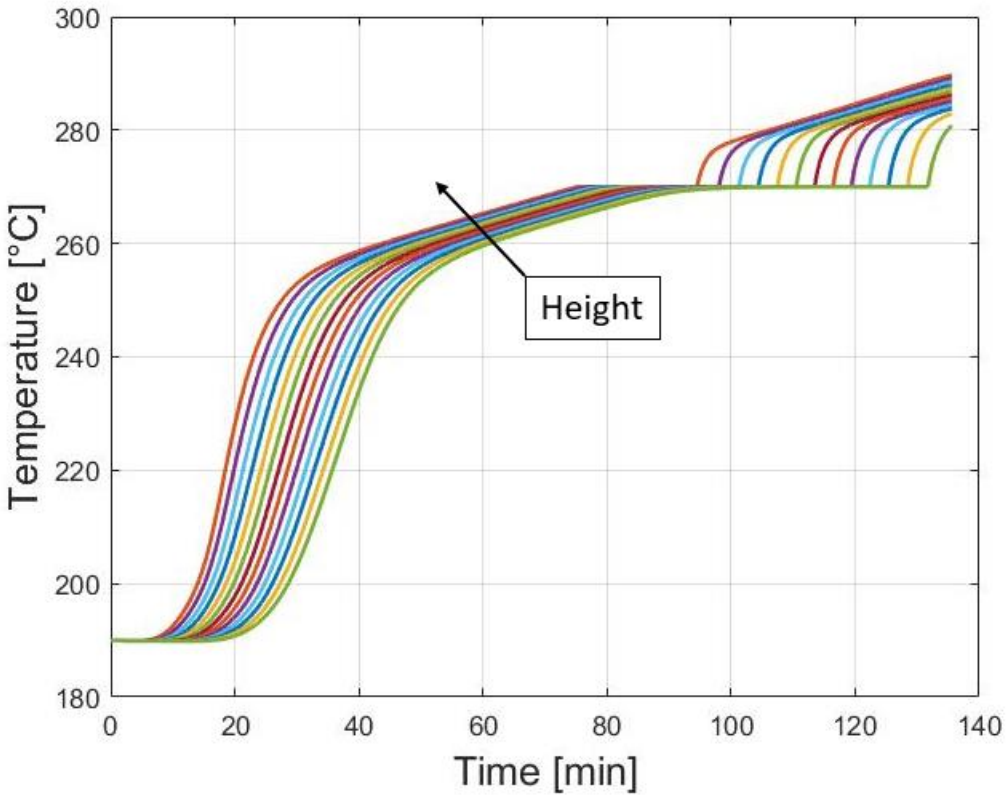

Figure 4.21 Time evolution of the temperature of the phase change material as the height of the toroidal tubes varies.

Comparing the time *evolution of the salt temperature* for different heights from the tank bottom, the differences caused by the introduction of PCMs are clearly visible (**Figure 4.22.a**) in relation to the evolution without them (**Figure 4.22.b**). *Plateaus* appears in the curves at the melting temperature of the PCM (270°C), with the exception of the top curve, which is above the tube bank and, consequently, is not affected by PCM inserts. At the end of the phase transition, the PCM temperature rises again. During the charge phase, the salts temperature increases progressively starting from the top to the layers below. This determines that the uppermost row of the tube bank is the first that starts (and completes)

the change of phase, the others rows follows on the base of their height from the tank bottom.

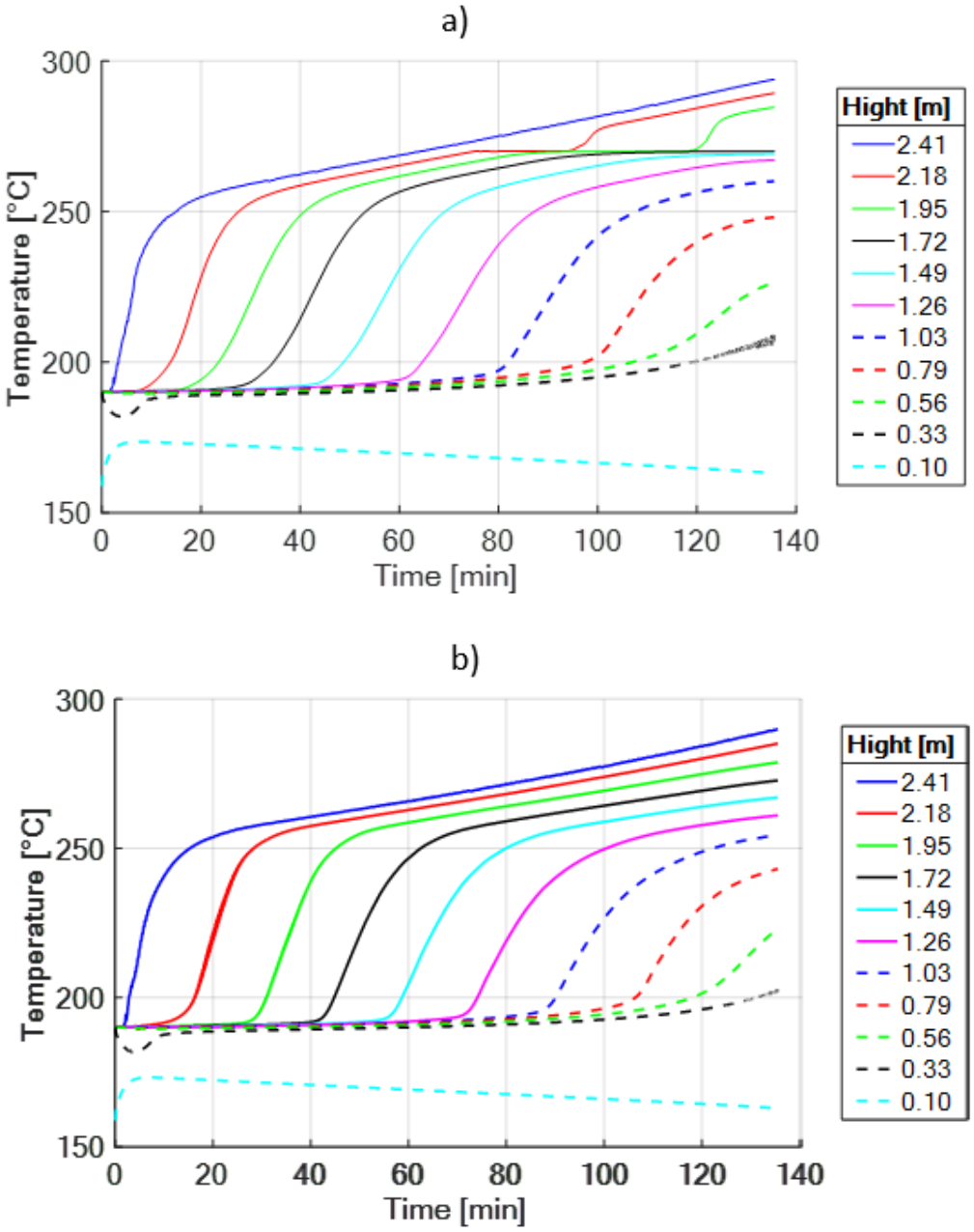

Figure 4.22 Evolution of salts temperature over time during the charging transient, for different heights from the tank base: a) storage system with PCM inserts and b) storage system without PCM inserts.

The *thermal stratification* of the salts inside the thermocline is shown in the **Figure 4.23** for the case with phase change inserts and in the **Figure 4.24** for the

Supervisors: Prof. Roberto Zanino - Dr. Mattia Cagnoli
Candidate: RICCARDO SISTI

case without them. In the region where the PCMs are located, a thermal gradient can be detected with temperatures everywhere higher than the melting temperature of the PCM. This is justified by the fact that the last row of tubes completes the phase transition about 3 minutes before the end of the transient. Immediately below the tube bank, a temperature step is established, which leads to a clear separation between the top of the tank, characterised by the highest temperatures, and the rest of the thermocline. At the base of this step, a temperature plateau can be observed, which corresponds to the melting temperature of the PCM (about 270 °C). It originates from the salts that passed through the PCM region in the minutes before the end of the transient, when the phase change material inserts were still accumulating latent heat at a constant temperature. This phenomenon shows how the phase change materials can stabilise the temperature of the salts around the melting temperature of the PCM.

The comparison between the two configurations (with and without the PCM inserts) shows that introducing the PCM allows increasing the salts temperature at the top of the tank of about 4 °C. However, also the salts temperature corresponding to the channel inlet section increases (about 2°C), therefore, the temperature difference at the channel ends increases of only 2 °C (+ 2%) by introducing the PCM.

Supervisors: Prof. Roberto Zanino - Dr. Mattia Cagnoli
Candidate: RICCARDO SISTI

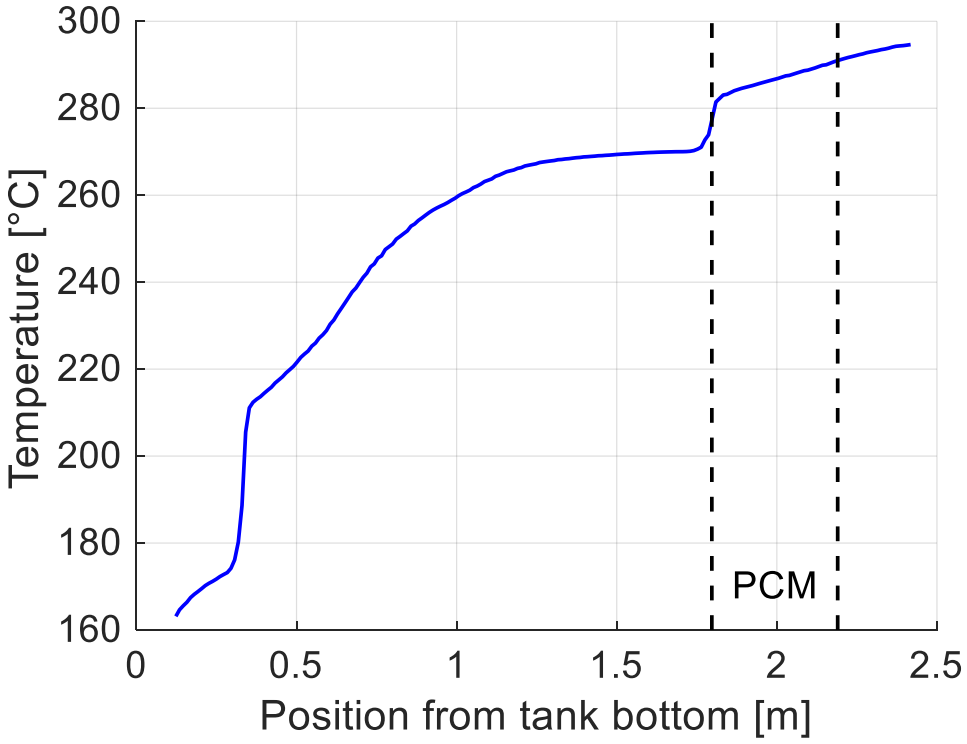

Figure 4.23 Thermal stratification of salts at the end of the charging transient in the configuration with PCM. Detail of the region where the inserts are located.

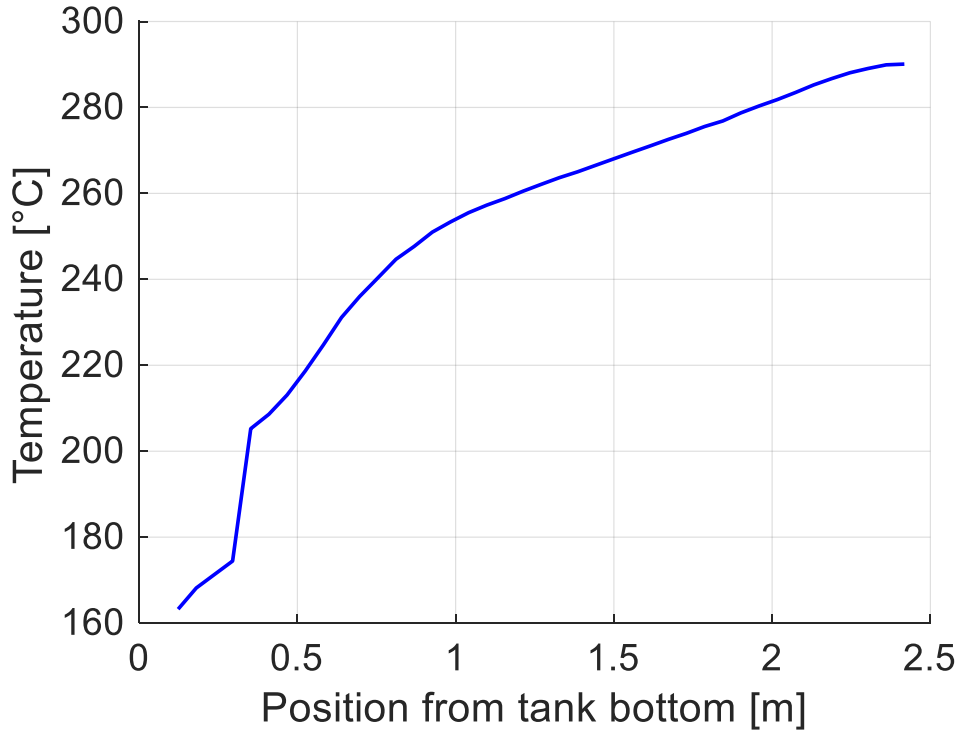

Figure 4.24 Thermal stratification of salts at the end of the charging transient in the configuration without PCM.

The last graph proposed (**Figure 4.25**), compares the temperature of the salts at the interface with the temperature of the PCMs relative to the first row of the tube bank. Here, it is possible to appreciate the influence of the variation of the PCMs heat transfer coefficient on the salts temperature during the transient. In the solid region, due to the thermal resistance offered by the low thermal conductivity of the PCM, a gap is established between the two temperatures. At the beginning of the phase transition, the heat transfer coefficient reaches its maximum value, this leads to a strong reduction of the temperature difference between the salts and the PCM. As a consequence of the increase of the liquid fraction inside the toroidal tubes and the temperature increase of the salts around the tubes over the time, the heat transfer coefficient is reduced, allowing the temperature of the salts to rise respect to the PCM's one until the end of the melting process. Finally, once the phase transition is completed, the temperature of the PCM in the toroidal tubes rises again, initially at a faster rate than the salts and then in a stable way, driven by the purely liquid heat transfer coefficient.

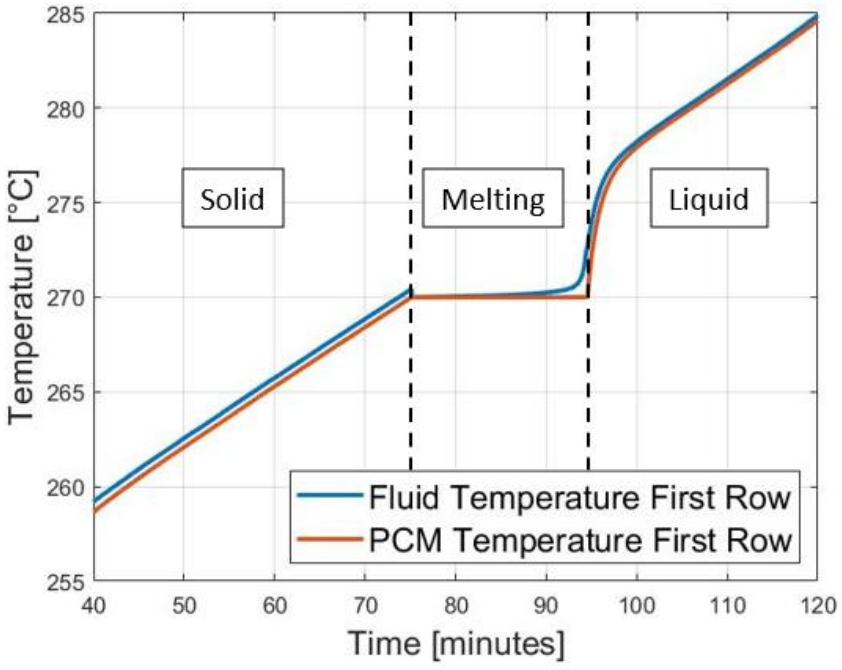

Figure 4.25 Detail of temperature evolution during the phase transition: comparison of salts temperature at toroidal tube interface and PCM temperature.

Supervisors:
Prof. Roberto Zanino - Dr. Mattia Cagnoli
Candidate:
RICCARDO SISTI

Chapter 5

5 Conclusions and Perspective

In this work a *numerical model* has been developed to reproduce the *behaviour* of an innovative thermocline storage system prototype proposed by ENEA as part of the ORC-Plus European project. The peculiarity of this prototype is the presence of a vertical channel, at the ends of which the charge and discharge heat exchangers are placed. The role of the channel is to preserve the thermal gradient of the tank during the charge and discharge phases.

This thesis was carried out following a previous thesis in which an axisymmetric CFD model of the thermocline storage system was developed and validated against experimental data. Starting from this model, the objective of the present thesis is to *numerically study* the potential improvement given by the introduction of inserts containing a phase change material (PCM) inside the thermocline storage system. Considering that the thermal energy storage is designed to supply an Organic Rankine Cycle (ORC), it was decided to couple the PCM melting temperature to the operative condition of the power system (>260°C). For this reason, the sodium nitrite (NaNO2) has been adopted, whose melting temperature of 270°C is well compatible with the temperature of the salts, which reach a maximum temperature of about 285°C according to the thermocline design.

The geometry of the inserts containing the phase change material corresponds to a tube bank composed of toroidal tubes arranged in staggered rows to form equilateral triangles. This configuration guarantees the best heat

Supervisors: Prof. Roberto Zanino - Dr. Mattia Cagnoli
Candidate: RICCARDO SISTI

exchange performance at low Reynolds numbers and allows the tank axisymmetry to be maintained. In addition, this geometry ensures the tubes to be placed at the desired height within the tank, enabling the positioning in the area where the expected temperature of the salts is close to the melting temperature of the PCMs. The tube bank was sized by means of a parametric analysis providing as results a configuration of 910 tubes arranged in 28 rows with a pitch to diameter ratio of 1.25 and an outer tube diameter of 13 mm (1 mm wall thickness).

The axisymmetric CFD model, developed in the previous thesis work, was modified to include the tube bank; however, the PCM and the tube wall are not included in the calculation domain. This choice was made because of the *high computational* cost in the physics proposed by *STAR-CCM+* to simulate phase change and the physics proposed is not suited for this specific case of study. The PCM and the tube wall have been replaced by a lumped parameter model, which solves the radial conduction in the pipe wall and the heat transfer with the PCM. This coupled CFD and lumped parameter model allowed simulating a charge transient and the results have been compared with those of the storage system without the PCM inserts. The outcomes show that the phase change material allows the temperature of the salts in the upper part of the tank to be stabilised, while also causing a clearer separation between the hot salts and the rest of the thermocline.

In perspective, the numerical model developed can be used to optimise the position and the geometry of the phase change material inserts, in order to exploit the potential offered by the stabilisation of the temperature of the salts obtained through the insertion of PCMs. In fact, an adequate sizing of the PCMs at mid-height would lead to a clear separation between the hot and cold salts, reproducing a configuration close to the double tank system (i.e. thermocline ideal condition). On the other hand, positioning the PCMs at the top or at the bottom would ensure not to violate the thermal limits of the generation or production systems coupled to the tank.

Appendix A

The results for the configurations with pitch to diameter equal to 1.5 and 2 are presented in the figures below.

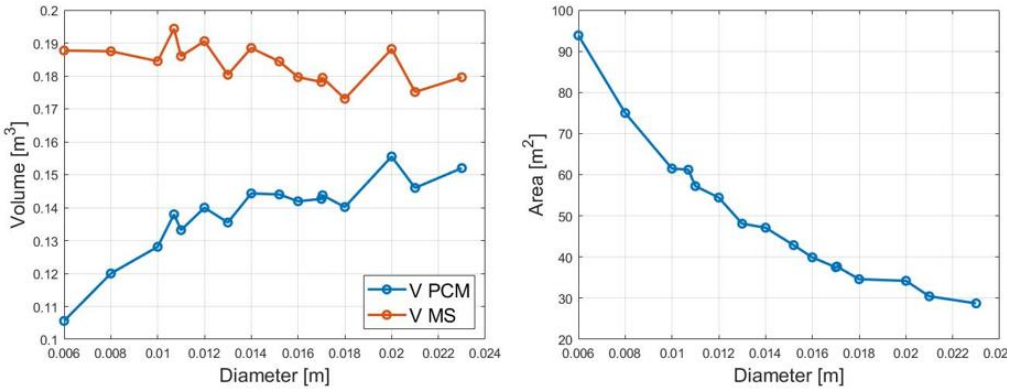

(a) (b)

Fig. 1 Pitch to diameter equal to 1.5: (a) introduced volume of PCM and (b) heat exchange area as a function of the external diameter of the tubes.

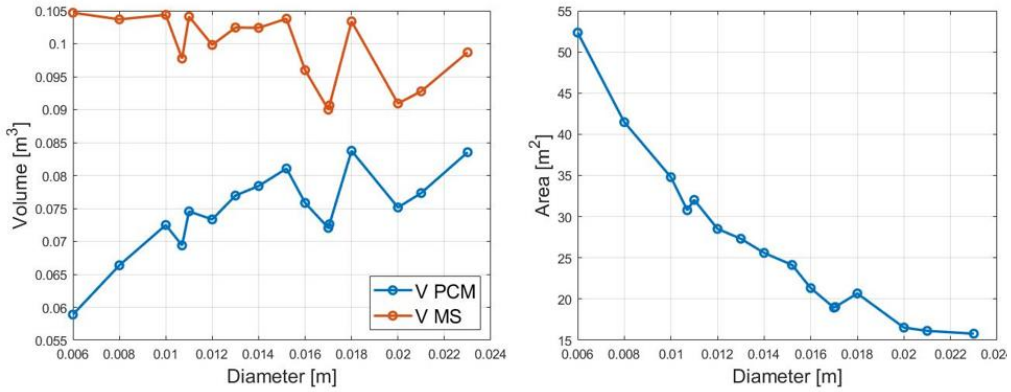

(a) (b)

Fig. 2 Pitch to diameter equal to 2: (a) introduced volume of PCM and (b) heat exchange area as a function of the external diameter of the tubes.

Supervisors: Prof. Roberto Zanino - Dr. Mattia Cagnoli
Candidate: RICCARDO SISTI

Appendix B

Within this section, the input data for each case study are presented in the table, while the benchmarking results between the Archibold model and the 0D model are presented in the figures below.

Tab. 1 Characteristic parameters for each case stud: internal radius of the shell, temperature difference between the wall and the PCM, dimensionless Stefan, Grashof and Prandtl numbers, thermal conductivity of the PCM and the wall and undercooling parameter.

Case	Ri	$T_w - T_m$	Gr	Pr	Ste	χ	ζ
	[m]	[°C]	$x10^4$				
1	0.010	5.0	1.32	8.98	0.048	0.966	0.0026
2	0.010	10.0	2.69	8.90	0.097	0.966	0.0026
3	0.010	15.0	4.13	8.81	0.145	0.966	0.0026
4	0.009	12.6	2.68	8.84	0.122	0.966	0.0026
5	0.011	7.5	2.66	8.93	0.072	0.966	0.0026
6	0.015	7.5	9.09	8.90	0.097	0.966	0.0026
7	0.020	10.0	21.50	8.90	0.097	0.966	0.0026
8	0.025	10.0	42.10	8.90	0.097	0.966	0.0026
10	0.020	10.0	21.50	8.90	0.097	0.671	0.0026
11	0.020	10.0	21.50	8.90	0.097	0.995	0.0026

Appendix B

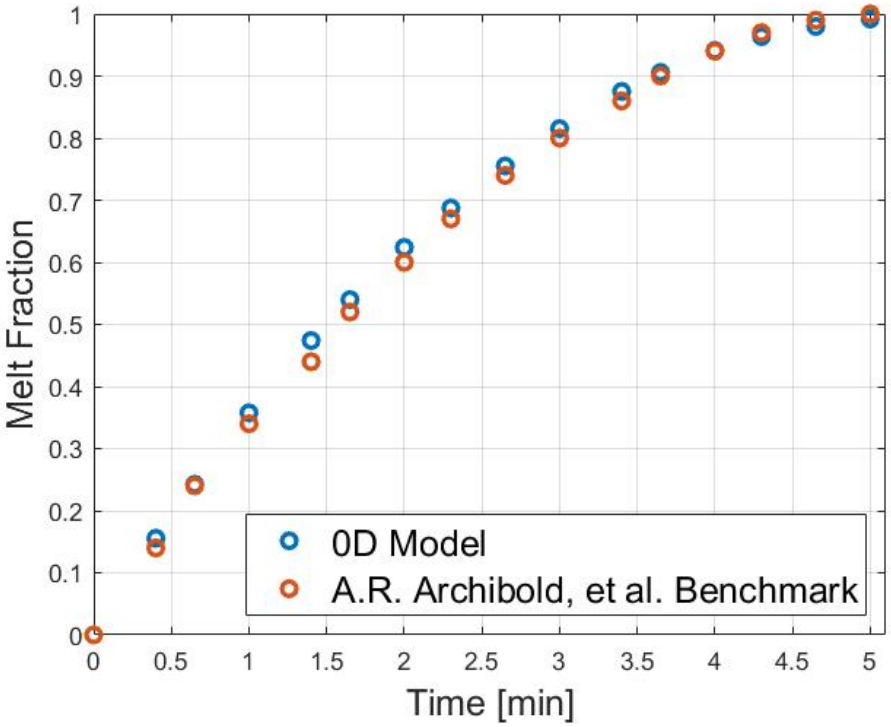

Fig. 3 Case 2.

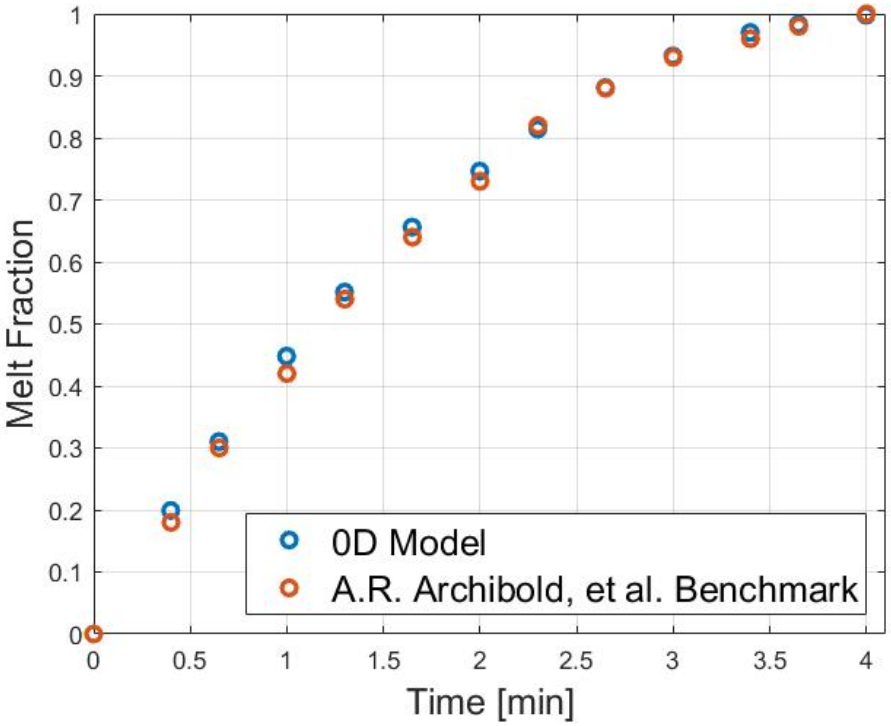

Fig. 4 Case 3.

Appendix B

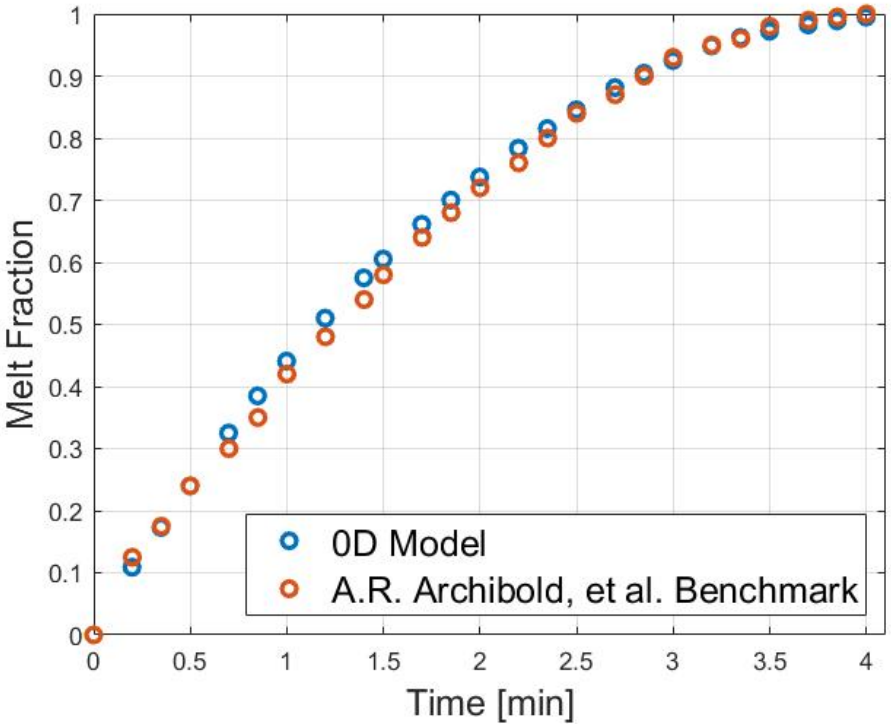

Fig. 5 Case 4.

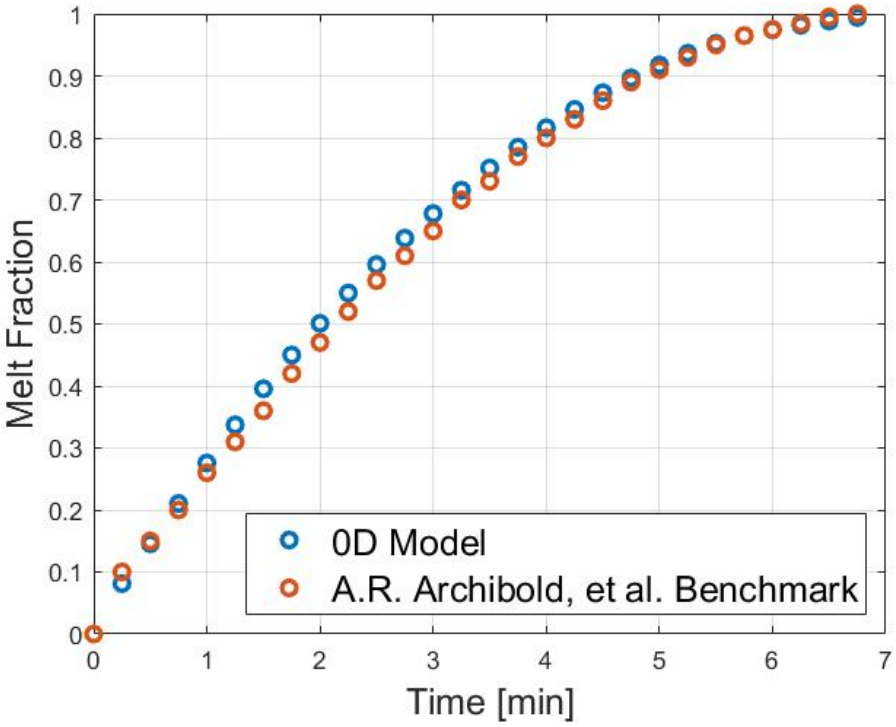

Fig. 6 Case 5.

Supervisors:
Prof. Roberto Zanino - Dr. Mattia Cagnoli
Candidate:
RICCARDO SISTI

Appendix B

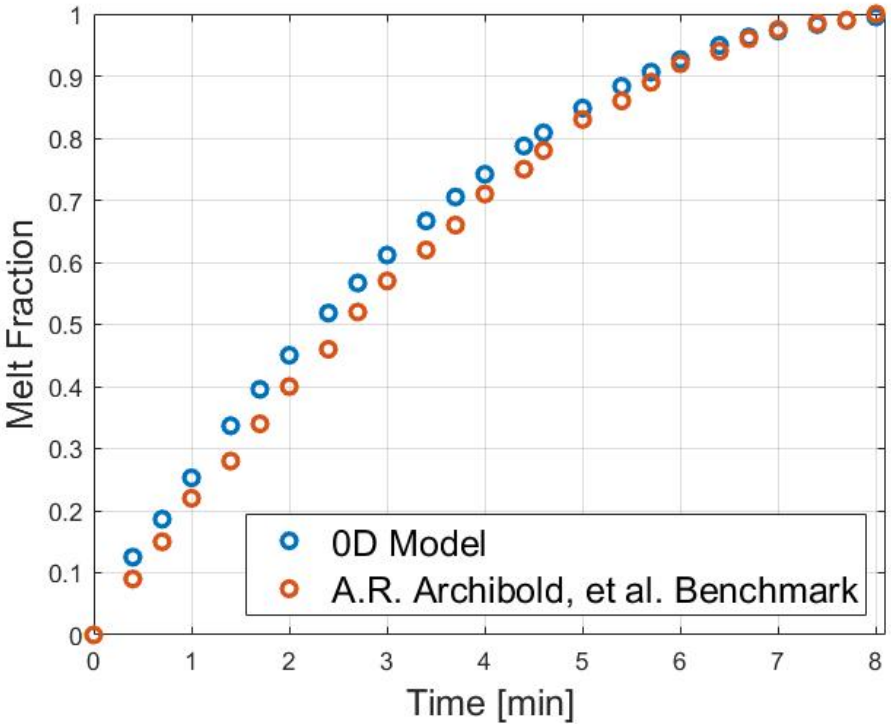

Fig. 7 Case 6.

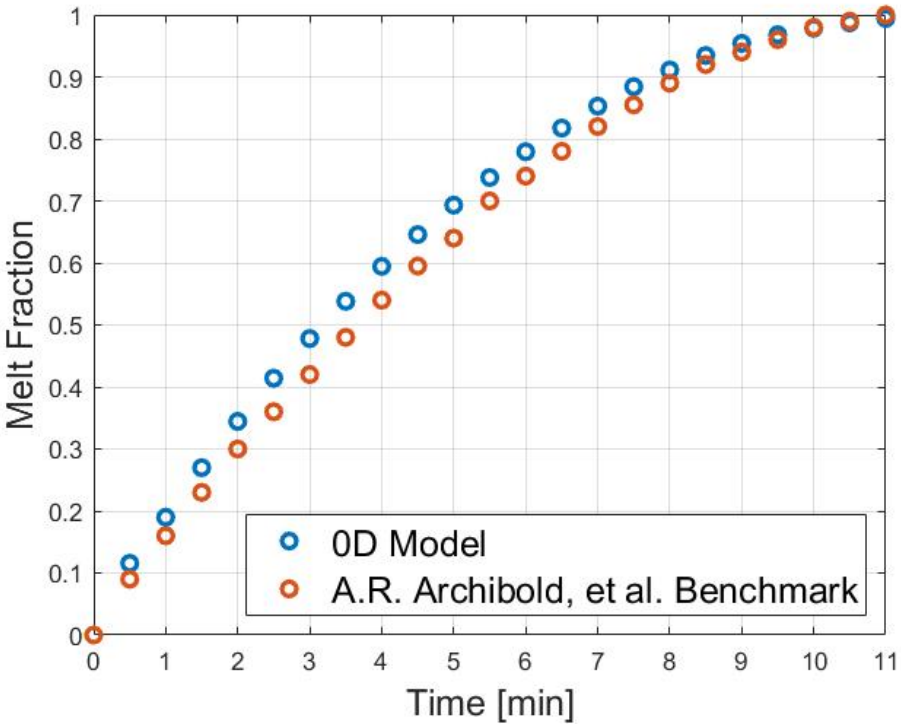

Fig. 8 Case 7.

Supervisors:
Prof. Roberto Zanino - Dr. Mattia Cagnoli
Candidate:
RICCARDO SISTI

Appendix B

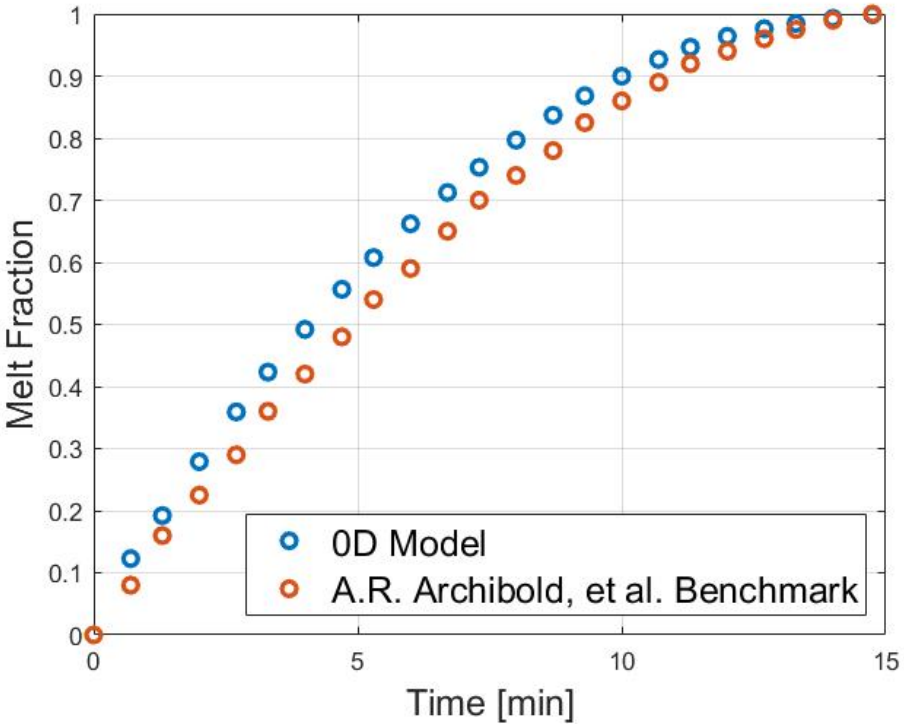

Fig. 9 Case 8.

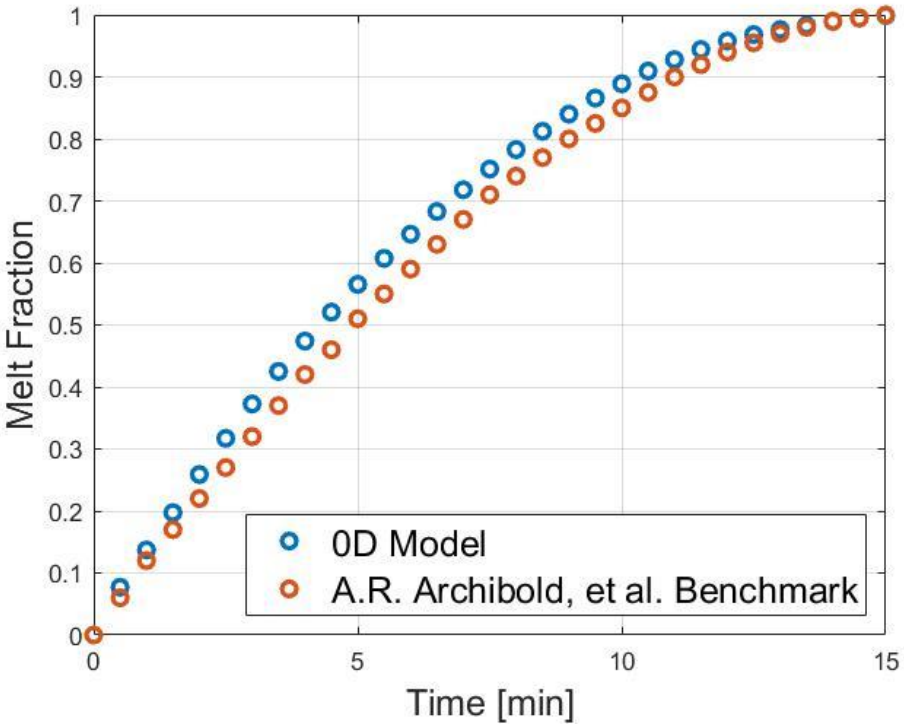

Fig. 10 Case 10.

Appendix B

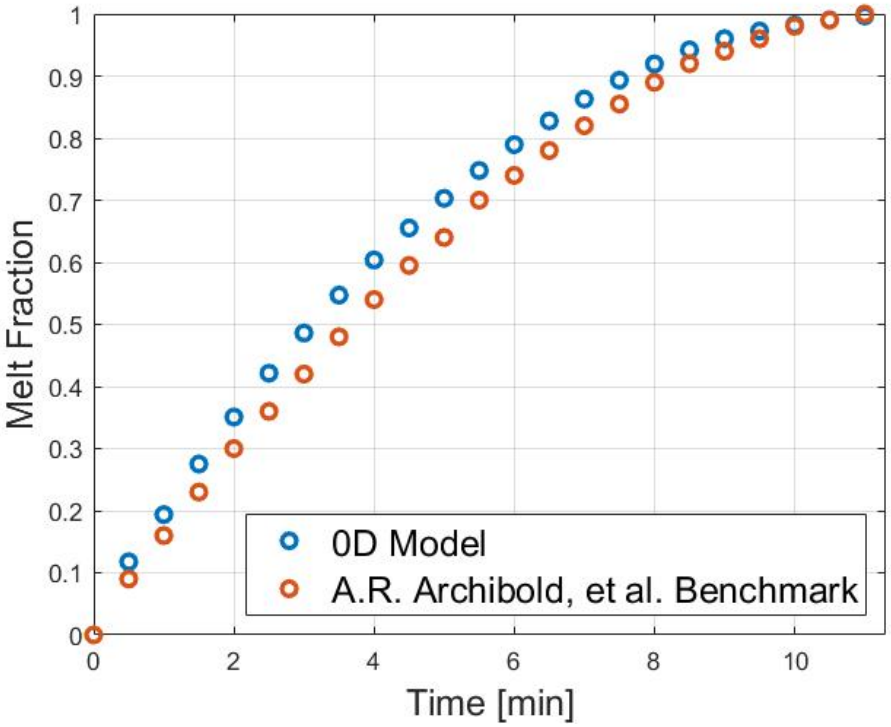

Fig. 11 Case 11.

Supervisors:
Prof. Roberto Zanino - Dr. Mattia Cagnoli
Candidate:
RICCARDO SISTI

Bibliography

[1] [Online]. Available: https://www.orc-plus.eu/. [Accessed 09 05 2021].

[2] IEA, "World Energy Outlook," Paris, 2019.

[3] F. Martins, C. Felgueiras and M. Smitková, "Fossil Fuel Energy Consumption in European Countries," *Energy Procedia,* vol. 153, pp. 107-111, 2018.

[4] [Online]. Available: https://unfccc.int/process-and-meetings/the-paris-agreement/the-paris-agreement/key-aspects-of-the-paris-agreement. [Accessed 07 09 2021].

[5] "World Energy Resources: Solar," in *World Energy Council*, 2013.

[6] IEA, "Renewables 2020 - Analysis and Forecast to 2025," 2020.

[7] J. Jorgenson, M. Mehos and P. Denholm, "Comparing the net cost of CSP-TES to PV deployed with battery storage," NREL, Denver, 2016.

[8] P. Denholm, M. O'Connell, G. Brinkman and J. Jorgenson, "Overgenerations from Solar Energy in California: A Field guide to the Duck Chart," NREL, Denver, 2015.

[9] S. J. Lewis, "Analysis and management of the impacts of a high penetration of photovoltaic systems in an electricity distribution network," in IEEE PES Innovative Smart Grid, Washington DC, 2011.

[10] J. Jorgenson, P. Denholm and M. Mehos, "Estimating the Value of Utility-Scale Solar Technologies in California under a 40% Renewable Portfolio Scenario," NREL, Denver, 2014.

[11] ESTELA, SolarPACES and Greenpeace International, "Solar Thermal Electricity Global Outlook," 2016.

[12] H. Yan, A. Wang, D. Chong, J. Liu and J. Yan, "Review on Performance Analysis of the Power Block in Concentrated Solar Power Plants," *Energy Technology,* vol. 9, 2021.

[13] I. Sarbu and C. Serbarchievici, "A Comprehensive Review of Thermal Energy Storage," *Sustainability,* vol. 10, 2018.

[14] U. Pelay, L. Luo, Y. Fan, D. Stitou and M. Rood, "Thermal Energy Storage System for Concentrated Solar Power Plants," *Renewable and Sustainable Energy Reviews,* vol. 79, 2017.

[15] S. Torras, C. D. Pérez-Segarra, I. Rodrìguez, J. Rigola and A. Oliva, "Parametric study of two-tank TES systems for CSP plants," *Energy Procedia ,* vol. 69, pp. 1049-1058, 2015.

[16] J. E. Kopp, "Two-tank indirect thermal storage designs for solar parabolic trough power plants," *Professional Papers and Capstones,* vol. 61, 2009.

[17] G. Angelini, A. Lucchini and G. Manzolini, "Comparison of thermocline molten salts storage performances to commercial two-tank configuration," *Energy Procedia,* vol. 49, pp. 694-704, 2014.

[18] J. Pacheco, S. K. Showalter and W. J. Kolb, "Development of a Molten-Salt Thermocline Thermal Storage System for Parabolic Trough Plants," *Journal of Solar Engineering,* vol. 124, pp. 123-153, 2002.

[19] M. A. Rosen, R. Tang and I. Dincer, "Effect of stratification on energy and exergy capacities in thermal storage systems," *Int. J. Energy Res.,* vol. 28, pp. 177-193, 2004.

[20] M. Falchetta, M. Binotti and F. Avallone, "Modelling thermocline storage for CSP yield assessment and process control simulation," in *AIP Conference Proceedings 2126*, 2019.

[21] S. D. Sharma and K. Sagara, "Latent Heat Storage Materials and Systems: A Review," *International Journal of Green Energy,* vol. 2:1, pp. 1-56, 2005.

[22] V. Russo, D. Mazzei and R. Liberatore, "Thermal energy storage with integrated heat exchangers using stratified molten salts system for 1 MWe CSP," in *AIP Conference Proceedings 2033*, 2018.

[23] W. Gaggioli, R. Liberatore, P. Di Ascenzi, D. Mazzei and V. Russo, "Experimental Test of Characterization of an Innovative Thermal Energy Storage System Based on Low Melting Molten Salt Thermocline Tank Integrated with an Oil Exchanger," in *SolarPaces*, 2019.

[24] S. Sau, E. Veca, N. Corsaro and G. Giorgi, "TESs materials characterization," 2015.

[25] I. Pellegrino, R. Zanino and M. Cagnoli , "Thermal-Fluid Dynamic Modelling of a Thermocline Storage System for CSP Applications," *Master Degree, Politecnico di Torino,* 2020.

[26] H. Versteeg and W. Malalasekera, An Introduction to Computational Fluid Dynamics - The finite volume method, Pearson Education Limited, 2007.

[27] A. Pizzolato, F. Donato, V. Verda and M. Santarelli, "CFD-based reduced model for the simulation of the thermocline thermal energy storage systems," *Applied Thermal Engineering,* vol. 76, pp. 391-399, 2015.

[28] F. P. Incropera, T. B. Bergman, A. S. Lavine and D. P. Dewitt, Introduction to Heat Transfer - Sixth Edition, John Wiley & Sons, 2011.

[29] J. H. Dieckmann , "Latent heat storage in concrete," Technische Universitat Kaiserslautern, 2006.

[30] S. Riffat, B. Mempouo and W. Fang, "Phase change material developments: a review," *International Journal of Ambient Energy,* 2013.

[31] A. Milozzi, A. Spadoni, E. Veca, S. Sau, R. Liberatore and M. Lanchi, "Selezione e caratterizzazione di sali e nanoparticelle per lo sviluppo di sistemi innovative a proprietà termiche incrementate e identificazione dei metodi di sintesi," Report RdS/PTR/083, 2019.

[32] H. E. S. Fath, "Heat exchanger performance for latent heat thermal energy storage system," *Energy Conversersion and Management,* vol. 31, pp. 149-155, 1991.

[33] P. A. Galione, C. D. Pérez-Segarra, I. Rodrìguez, O. Lehmkuhl and J. Rigola, "A new thermocline-PCM thermal storage concept for CSP plants. Numerical analysis and perspectives," *Energy Procedia,* vol. 49, pp. 790-799, 2014.

[34] [Online]. Available: https://www.marinispa.it/tubi/tubi-acciaio-inox. [Accessed 19 05 2021].

[35] Y. Q. Wang, L. A. Penner and S. J. Ormiston, "ANALYSIS OF LAMINAR FORCED CONVECTION OF AIR FOR CROSSFLOW IN BANKS OF STAGGERED TUBES," *Numerical Heat Transfer,* vol. 38, pp. 819-845, 2010.

[36] S. D. Industries, Simcenter User Guide, Simens, 2021.

[37] A. D. Brent, V. R. Voller and K. J. Reid, "Enthalpy-porosity technique for modeling convection diffusion phase change: application to the melting of a pure metal," *Numerical Heat Transfer,* vol. 13, pp. 297-318, 1988.

[38] E. Assis, L. Katsman, G. Ziskind and R. Letan, "Numerical and experimental study of melting in a spherical shell," *International Journal of Heat and Mass Transfer,* vol. 50, 2007.

[39] D. R. Oliver, "The effect of natural convection on viscous-flow heat transfer in horizontal tubes," *Chem. Eng. Sci.,* vol. 17, pp. 335-350, 1962.

[40] M. Rouhani and M. Bahrami, "Improved Lumped Parameter Model for Phase Change in Latent Thermal Energy Storage System," in *IX Minsk International Seminar*, Minsk, 2015.

[41] P. Jany and A. Bejan, "Scaling theory of melting with natural convection in an enclosure," *int. J. Heat Mass Transfer,* vol. 31, 1987.

[42] A. R. Archibold, M. M. Rahman, D. Y. Goswami and E. K. Stefanakos, "Analysis of heat transfer and fluid flow during melting inside a spherical container for thermal energy storage," *Applied Thermal Engineering,* vol. 64, pp. 396-407, 2014.

[43] R. Liberatore, M. Falchetta, W. Gaggioli, D. Mazzei and V. Russo, "Power production of an ORC system using a stratified molten salt as thermal energy storage integrated in a CSP plant," in AIP Conference Proceedings 2126, 2019.